

Domain-decomposition least-squares Petrov–Galerkin (DD-LSPG) nonlinear model reduction

Chi Hoang*

Youngsoo Choi[†]Kevin Carlberg[‡]

Abstract

A novel domain-decomposition least-squares Petrov–Galerkin (DD-LSPG) model-reduction method applicable to parameterized systems of nonlinear algebraic equations (e.g., arising from discretizing a parameterized partial-differential-equations problem) is proposed. In contrast with previous works, we adopt an algebraically non-overlapping decomposition strategy rather than a spatial-decomposition strategy, which facilitates application to different spatial-discretization schemes. Rather than constructing a low-dimensional subspace for *the entire state space* in a monolithic fashion, the methodology constructs separate subspaces for the different subdomains/components characterizing the original model. During the offline stage, the method constructs low-dimensional bases for the interior and interface of subdomains/components. During the online stage, the approach constructs an LSPG reduced-order model for each subdomain/component (equipped with hyper-reduction in the case of nonlinear operators), and enforces strong or weak compatibility on the ‘ports’ connecting them. We propose several different strategies for defining the ingredients characterizing the methodology: (i) four different ways to construct reduced bases on the interface/ports of subdomains, and (ii) different ways to enforce compatibility across connecting ports. In particular, we show that the appropriate compatibility-constraint strategy depends strongly on the basis choice. In addition, we derive *a posteriori* and *a priori* error bounds for the DD-LSPG solutions. Numerical results performed on nonlinear benchmark problems in heat transfer and fluid dynamics that employ both finite-element and finite-difference spatial discretizations demonstrate that the proposed method performs well in terms of both accuracy and (parallel) computational cost, with different choices of basis and compatibility constraints yielding different performance profiles.

Keywords: domain decomposition, substructuring, model reduction, least-squares Petrov–Galerkin projection, error bounds

1 Introduction

Many tasks in computational science and engineering are *many query* in nature, as they require the repeated simulation of a parameterized large-scale computational model. Model reduction has become a popular approach to make such tasks tractable. Most of such techniques first perform an “offline” training stage that simulates the computational model for multiple input-parameter instances; then, during an “online” deployed stage, these techniques reduce the dimensionality and complexity of the original computational model at arbitrary input-parameter instances by performing a projection process of the original computational model onto a low-dimensional subspace or manifold.

While such reduced-order models (ROMs) have demonstrated success in many applications, challenges arise when applying model reduction either to *extreme-scale models* or to *decomposable systems*, i.e., systems

*Extreme-scale Data Science and Analytics Department, Sandia National Laboratories, Livermore, CA 94550 (ckhoang@sandia.gov). Sandia National Laboratories is a multimission laboratory managed and operated by National Technology and Engineering Solutions of Sandia, LLC, a wholly owned subsidiary of Honeywell International, Inc., for the U.S. Department of Energy’s National Nuclear Security Administration under contract DE-NA-0003525.

[†]Lawrence Livermore National Laboratory, Livermore, CA 94550 (choi15@llnl.gov). Lawrence Livermore National Laboratory is operated by Lawrence Livermore National Security, LLC, for the U.S. Department of Energy, National Nuclear Security Administration under Contract DE-AC52-07NA27344 (LLNL-JRNL-812648).

[‡]Mechanical Engineering and Applied Mathematics, University of Washington, Seattle, WA 98195 (ktcarlb@uw.edu).

composed of well-defined components. In the former case, the extreme-scale nature of the original computational model renders the offline training simulations infeasible. In the latter case, the many-query task often involves design, wherein components are swapped or their interconnecting topology is modified; in this case, the state space characterizing the original computational model changes substantially between queries, rendering training simulations (which assume a fixed state space) challenging.

To date, researchers have developed several methods to enable model reduction for decomposable systems. During the offline stage, these approaches construct a unique reduced basis for each component; during the online stage, they formulate a reduced-order model for the full system using domain-decomposition approaches that enforce solution compatibility along component interfaces. Most approaches to date have been developed for parameterized *linear* partial differential equations (PDEs).

Reduced basis element (RBE) methods, which comprise a family of domain-decomposition reduced-order model (DDROM) techniques, are applicable to *linear* PDEs [1, 2, 3, 4, 5, 6]. Maday et al. [1, 2] proposed the very first work of this family; this approach combines the reduced-basis (RB) method with domain decomposition (DD), using full-subdomain bases¹ and “gluing” the subdomain interfaces weakly via Lagrange multipliers. The full-subdomain bases are built in the offline stage, while in the online stage a saddle point problem [7] is solved to compute the solution for any input-parameter instance. The reduced basis hybrid method (RBHM), which was proposed later by Iapichino and coworkers [3], modifies the RBE by including the finite element (FE) coarse solutions in the reduced bases (in the online stage) to recover the nonzero normal stress component of the final solution. The RBE and RBHM were employed to solve the steady Stokes problem with applications in cardiovascular networks [1], [3]. In the reduced-basis–domain-decomposition–finite-element (RDF) method [6], the same authors proposed to separate the global DOFs into all subdomain interior DOFs and “skeleton” DOFs, then approximate all subdomain interior DOFs by RB method. The unknowns in the final reduced linear system comprise the generalized coordinates associated with all subdomain interiors and FE degrees of freedom on the skeleton. Similar in concept, the static condensation reduced basis element (SCRBE) method proposed by Huynh et al. [4, 8] decomposes the “skeleton” DOFs further into “port” DOFs on each subdomain, where a subdomain can have multiple nonoverlapping ports. SCRBE employs a primal-Schur domain-decomposition method to assemble and solve the resulting system. In particular, Ref. [4] carefully constructs interface bases to represent *all possible variations* of the solution on the skeleton of the global domain. While this is a robust and comprehensive approach to compute the skeleton solution, it also incurs a high computational cost: the dimension of the Schur-complement system is equal to the number of FE degrees of freedom across all ports, which can remain large scale for fine spatial discretizations. To address this, Ref. [5] applies “adaptive port reduction” to reduce the number of port degrees of freedom and hence the dimensionality and cost of solving the Schur-complement system. While the majority of the work on RBE deals with linear PDEs, we are aware that there is at least one work that deals with nonlinear PDEs [9].

Besides the RBE family mentioned above, researchers have developed other DDROM methods to solve parameterized linear PDEs in the context of multiscale heterogeneous materials analysis. These methods include the multiscale reduced basis method (MsRBM) [10], FE²-based model order reduction method [11], the localized reduced basis multiscale method (LRBMS) [12, 13], the reduced basis localized orthogonal decomposition method (RB-LOD) [14], the reduced basis method for heterogeneous domain decomposition (RBHDD) [15] and recently the ArbiLoMod method [16]. In addition, we are also aware of the use of DDROM in the work of graphic community, for example (not a comprehensive list), [17, 18] deal with nonlinear problems while [19, 20] handle linear problems. The work [21] solves nonlinear problems using a FOM-ROM hybrid approach that will be described in next paragraph.

While some DDROM techniques have been applied to nonlinear PDEs, most of these techniques are multiscale in nature, meaning that they apply a ROM to only a *subset* of the physical domain, and apply the high-fidelity model elsewhere; compatibility between the ROM and high-fidelity-model solutions is enforced using non-overlapping domain decomposition methods and some multiscale homogenization assumptions [11]. For example, in the work by Buffoni and coworkers [22], the authors implemented the overlapping

¹Note that “full-subdomain bases” here include all degrees of freedom (DOFs) of a subdomain: both interior and interface DOFs.

classical Schwarz method (using Dirichlet–Neumann iterations [23]) and divided the computational domain into two subdomains. The high-fidelity-model subdomain is discretized using a standard method (e.g., finite difference, finite element), while the ROM subdomain employs a snapshot-based proper orthogonal decomposition (POD) technique [24] with subdomain bases. Solution compatibility on the interface holds weakly through the enforcement of continuity of normal derivatives of the trace of the solutions on the interface. In another work by Kerfriden et al. [25], the authors used a primal-Schur domain-decomposition method combined with a snapshot-based POD ROM subdomain to solve nonlinear fracture-mechanics problems. In particular, the approach approximates the interior DOFs of *linear subdomains* with snapshot-POD (further reduction with the hyper-reduction technique DEIM [26] due to nonaffine parameter dependence) and use a full-order model (FOM) on nonlinear damaged subdomains. The Schur-complement system is formed by enforcing strong (i.e., node pairwise) compatibility between ROM and FOM subdomains and condenses out only the generalized coordinates characterizing the ROM subdomains, rendering the Schur-complement system high-dimensional. With similar FOM/ROM hybrid idea, the DD-POD method [27] uses the Gravouil–Combescure domain-decomposition approach [28] to solve elastic–plastic structural dynamics problems. The method divides the domain of interest into subdomains; during the online stage, a plastic check is performed on each subdomain to determine whether ROM or FOM approximations will be implemented in that subdomain. Again, full-subdomain bases are used in the linear-elastic subdomains and weak compatibility constraints are used on the interface. Baiges and coworkers [29] used a primal-dual monolithic approach to solve incompressible Navier–Stokes equations with overlapping domain decomposition. The approach also comprises a FOM/ROM hybrid wherein the physical domain is decomposed into FOM, ROM and overlapping subdomains. The ROM subdomains use full-subdomain bases and are further hyper-reduced by a discrete variant [30] of the best point interpolation method, while the overlapping/interface regions enforce velocity continuity, which corresponds to a weak compatibility constraint.

This work aims to overcome several shortcomings of existing works. First, *most* available DDROM methods for nonlinear PDEs employed a hybrid ROM/FOM approach; a “complete ROM” methodology appears to be missing for nonlinear problems (except the work [9], to the best of our knowledge). Second, most previously developed DDROM methods were applied to self-adjoint problems and thus constrained optimization problems could be derived from a Galerkin-projection perspective; the extension of many methods to non-self-adjoint problems is unclear. Finally, most of the above approaches (with the exception of SCRBE [4, 8]) employ “full-subdomain” bases with support over both interior and interface degrees of freedom. Such bases only are generally compatible only with weak constraints (see, e.g., [1, 3, 22, 27]), which precludes an equivalent global solution due to non-uniqueness of the solution on the interfaces. To address these shortcomings, this work is characterized by the following novel features, which, we believe, are valuable steps toward addressing the challenges arose from the nonlinear extreme-scale models (although we do not demonstrate our numerical results on a extreme-scale problem):

- We consider parameterized systems of nonlinear algebraic equations, and adopt an algebraically non-overlapping decomposition strategy rather than a spatial-decomposition strategy, which facilitates application to models derived using different discretization methods.
- We develop a “complete ROM” approach that applies model reduction to all degrees of freedom characterizing the nonlinear algebraic system; thus it is not a ROM/FOM hybrid.
- We formulate a constrained optimization problem for the global problem by equipping the least-squares Petrov–Galerkin (LSPG²) [31, 32, 33, 34, 35, 36] projection (with hyper-reduction [37, 38]) with interface-compatibility constraints. We employ a sequential quadrating programming (SQP) method to solve the resulting optimization problem. Critically, this formulation is valid for both self-adjoint and non-self-adjoint problems.
- We propose four different subdomain basis types, including the classical “full-subdomain” type and three “interface/boundary” types: port, skeleton, and full-interface. Consequently, the characterization of the solution on the interfaces has much greater flexibility than in previous contributions.

²For communities other than model reduction one, LSPG and ‘minimum residual’ are completely equivalent.

- Support for both strong and weak compatibility constraints on the interfaces for all basis types. In particular, we show that the best choice for compatibility constraints is strongly dependent on the subdomain-basis type (i.e., weak compatibility is best for full-subdomain and full-interface bases; strong compatibility is best for port and skeleton bases).
- Both *a posteriori* and *a priori* error bounds for the method, which illustrate how the error on each subdomain and port can be bounded using global quantities.
- Bottom-up (or subdomain) training (to be distinguished with top-down training bases above) is proposed (although still simple and not yet mature) and pave the way toward handling nonlinear extreme-scale models and decomposable systems.
- Numerical experiments on benchmark problems in heat transfer and fluid dynamics that employ both finite-element and finite-difference discretizations that systematically assess the effect of all method parameters on accuracy and computational cost, lending deep insights into the performance aspects of the proposed methodology.

The paper is structured as follows. Section 2 formulates the full-order model and algebraically non-overlapping decomposition that characterizes our domain-decomposition strategy. Section 3 describes the proposed DD-LSPG framework, including the two proposed choices for subdomain reduced bases (Sections 3.1 and 3.2), and strong vs. weak compatibility constraints (Section 3.3). Section 4 describes the proposed SQP solver used to numerically solve the constrained optimization problem characterizing DD-LSPG projection, its particularization to the two types of subdomain reduced bases (Sections 4.1 and 4.2) and its serial/parallel costs (Section 5). Section 6 describes the offline algorithms for constructing interior/boundary bases (Section 6.1) and full-subdomain bases (Section 6.2). Section 7 derives *a posteriori* and *a priori* error bounds for the method. Section 8 reports numerical experiments on a benchmark problem in heat transfer that employs a finite-element discretization (Section 8.1) and a benchmark problem in fluid dynamics that employs a finite-difference discretization (Section 8.2). Finally, Section 9 concludes the paper.

2 Domain-decomposition formulation

We consider the (high-fidelity) full-order model to be expressed as a parameterized system of nonlinear algebraic equations

$$\mathbf{r}(\mathbf{x}; \boldsymbol{\mu}) = \mathbf{0}, \quad (2.1)$$

where the residual $\mathbf{r} : \mathbb{R}^n \times \mathcal{D} \rightarrow \mathbb{R}^n$ is nonlinear in (at least) its first argument, $\boldsymbol{\mu} \in \mathcal{D} \subseteq \mathbb{R}^{n\mu}$ denotes the parameters, and $\mathbf{x} : \mathcal{D} \rightarrow \mathbb{R}^n$ denotes the state, which is implicitly defined as the solution to Eq. (2.1) given an instance of the parameters. Such problems arise, for example, after applying spatial discretization to a stationary PDE problem; because we take Eq. (2.1) to be our full-order model, our methodology is *spatial-discretization agnostic*. For notational simplicity, we suppress all dependence on the parameters $\boldsymbol{\mu}$ until needed in Section 6.

We consider an *algebraic decomposition* of this problem into $n_\Omega (\leq n)$ ‘subdomains’ such that the residual satisfies

$$\mathbf{r} : \mathbf{w} \mapsto \sum_{i=1}^{n_\Omega} [\mathbf{P}_i^r]^T \mathbf{r}_i(\mathbf{P}_i^\Omega \mathbf{w}, \mathbf{P}_i^\Gamma \mathbf{w}), \quad \forall \mathbf{w} \in \mathbb{R}^n. \quad (2.2)$$

Here, $\mathbf{r}_i : \mathbb{R}^{n_i^\Omega} \times \mathbb{R}^{n_i^\Gamma} \rightarrow \mathbb{R}^{n_i^r}$ with $\mathbf{r}_i : (\mathbf{w}_i^\Omega, \mathbf{w}_i^\Gamma) \mapsto \mathbf{r}_i(\mathbf{w}_i^\Omega, \mathbf{w}_i^\Gamma)$ denotes the i th subdomain residual, $\mathbf{P}_i^r \in \{0, 1\}^{n_i^r \times n}$ denotes i th the residual sampling matrix, $\mathbf{P}_i^\Omega \in \{0, 1\}^{n_i^\Omega \times n}$ denotes the i th interior-state sampling matrix, and $\mathbf{P}_i^\Gamma \in \{0, 1\}^{n_i^\Gamma \times n}$ denotes the i th interface-state sampling matrix; each sampling matrix comprises selected rows of the $n \times n$ identity matrix. The residual sampling matrix is such that the decomposition is *algebraically non-overlapping*, i.e., $\mathbf{P}_i^r [\mathbf{P}_j^r]^T = \mathbf{0}$ for $i \neq j$ and $\sum_{i=1}^{n_\Omega} n_i^r = n$. Further, the interior-state sampling matrix satisfies $\mathbf{P}_i^\Omega [\mathbf{P}_j^\Omega]^T = \mathbf{0}$ for $i \neq j$; this implies that there is no overlap between

the interior states associated with different subdomains. Thus, the operators \mathbf{P}_i^Ω and \mathbf{P}_i^Γ , $i = 1, \dots, n_\Omega$ are determined from the sparsity patterns of the sampled Jacobians $\mathbf{P}_i^r \frac{\partial \mathbf{r}}{\partial \mathbf{w}}$, $i = 1, \dots, n_\Omega$. We define the total number of degrees of freedom for each subdomain as $n_i := n_i^\Omega + n_i^\Gamma$; note that $n_i \geq n_i^r$.

If we set $\mathbf{x}_i^\Omega := \mathbf{P}_i^\Omega \mathbf{x} \in \mathbb{R}^{n_i^\Omega}$ and $\mathbf{x}_i^\Gamma := \mathbf{P}_i^\Gamma \mathbf{x} \in \mathbb{R}^{n_i^\Gamma}$, then from Eqs. (2.1)–(2.2), the solution for each subdomain $\mathbf{x}_i := (\mathbf{x}_i^\Omega, \mathbf{x}_i^\Gamma)$ satisfies

$$\mathbf{r}_i(\mathbf{x}_i^\Omega, \mathbf{x}_i^\Gamma) = \mathbf{0}, \quad i = 1, \dots, n_\Omega \quad (2.3)$$

along with compatibility conditions that enforce consistency across the boundary states for different subdomains. To reason about these compatibility conditions, we define a set of n_p ‘ports’; the j th port is characterized by $n_j^p \leq n$ states that are shared across a fixed set of subdomains denoted by $P(j) \subseteq \{1, \dots, n_\Omega\}$. Then, the compatibility conditions can be expressed as

$$\mathbf{P}_i^j \mathbf{x}_i^\Gamma = \mathbf{P}_\ell^j \mathbf{x}_\ell^\Gamma, \quad i, \ell \in P(j), \quad j = 1, \dots, n_p, \quad (2.4)$$

where the port sampling matrix $\mathbf{P}_i^j \in \{0, 1\}^{n_j^p \times n_i^\Gamma}$ comprises selected rows of the $n_i^\Gamma \times n_i^\Gamma$ identity matrix. For a given subdomain i , we require the ports to be non-overlapping such that $\mathbf{P}_i^j [\mathbf{P}_i^\ell]^T = \mathbf{0}$ for $j, \ell \in Q(i)$ and $j \neq \ell$ and $\sum_{j \in Q(i)} n_j^p = n_i^\Gamma$, where we have defined the set of ports associated with subdomain i as $Q(i) := \{j \mid i \in P(j)\} \subseteq \{1, \dots, n_p\}$. We note that for a given port j , although the number of *total* pairwise compatibility conditions arising from Eq. (3.3) is $\binom{k}{2}$, the number of *unique* pairwise compatibility conditions is only $n_j^{\text{pair}} := |P(j)| - 1$. Using this formulation, the full-order model (2.1) can be recast in decomposed form as

$$\begin{aligned} \mathbf{r}_i(\mathbf{x}_i^\Omega, \mathbf{x}_i^\Gamma) &= \mathbf{0}, \quad i = 1, \dots, n_\Omega \\ \sum_{i=1}^{n_\Omega} \bar{\mathbf{A}}_i \mathbf{x}_i^\Gamma &= \mathbf{0}, \end{aligned} \quad (2.5)$$

where $\bar{\mathbf{A}}_i \in \{-1, 0, 1\}^{n_{\bar{A}} \times n_i^\Gamma}$ with $n_{\bar{A}} = \sum_{j=1}^{n_p} n_j^{\text{pair}} n_j^p$ denote the constraint matrices associated with port-compatibility conditions (3.3). Note that Eqs. (2.5) comprise $\sum_{i=1}^{n_\Omega} n_i^r + n_{\bar{A}} = n + n_{\bar{A}}$ equations in $\sum_{i=1}^{n_\Omega} n_i^\Omega + \sum_{i=1}^{n_\Omega} n_i^\Gamma$ unknowns; as there exists a unique solution to these equations³, we have $n + n_{\bar{A}} \geq \sum_{i=1}^{n_\Omega} n_i^\Omega + \sum_{i=1}^{n_\Omega} n_i^\Gamma$.

For illustration, Figure 1 shows an example of a decomposition using $n_\Omega = 4$ subdomains and $n_p = 5$ global ports for the case of a full-order model derived from discretizing a PDE in two spatial dimensions using a residual operator with a 9-point stencil. Figure 2 shows the degrees of freedom and residual elements associated with subdomain Ω_1 .

3 Domain decomposition least-squares Petrov–Galerkin (DD-LSPG) projection

We now consider applying least-squares Petrov–Galerkin (LSPG) model reduction [31, 32, 33, 34] in the domain-decomposition setting presented in Section 2.

3.1 Interior/boundary bases

Assume we have constructed interior reduced bases $\Phi_i^\Omega \in \mathbb{R}_*^{n_i^\Omega \times p_i^\Omega}$ with $p_i^\Omega \leq n_i^\Omega$, $i = 1, \dots, n_\Omega$ and interface reduced bases $\Phi_i^\Gamma \in \mathbb{R}_*^{n_i^\Gamma \times p_i^\Gamma}$ with $p_i^\Gamma \leq n_i^\Gamma$, $i = 1, \dots, n_\Omega$, where $\mathbb{R}_*^{m \times n}$ denotes the non-compact Stiefel manifold: the set of full-column-rank $m \times n$ real-valued matrices; Section 6 described proposed approaches for constructing these bases. We then approximate the solution on the i th subdomain in the associated

³With the assumption that equation (2.1) is well-posed.

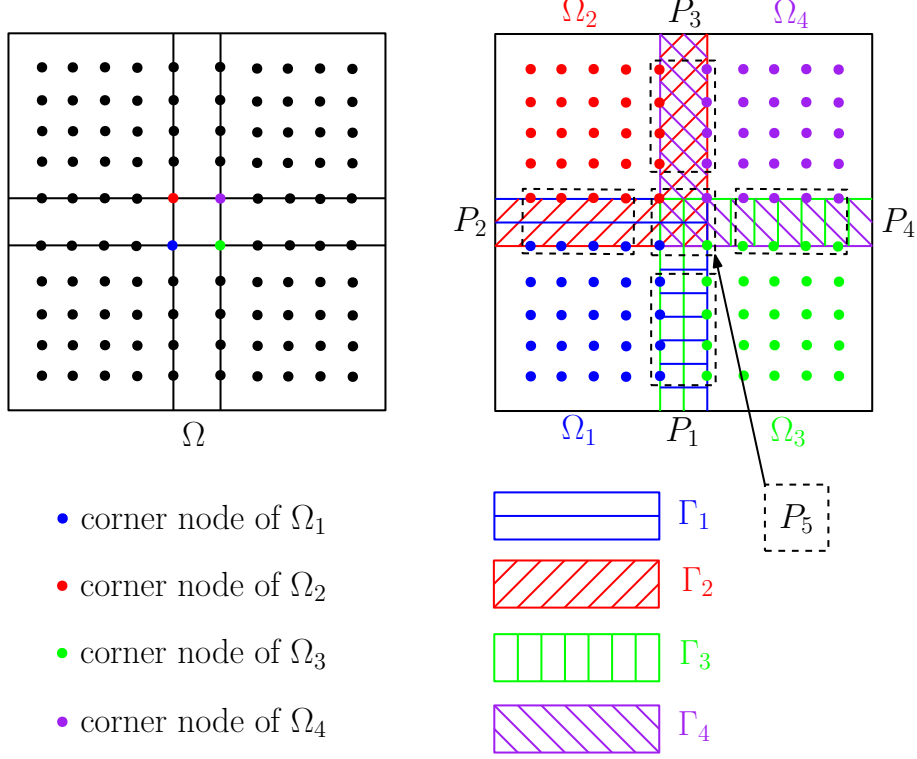


Figure 1: Domain-decomposition example: full-order model derived from discretizing a PDE in two spatial dimensions using a residual operator with a 9-point stencil. (Left) Residual and corner nodes. (Right) Each colored point is associated with a residual for the associated subdomain, $n_\Omega = 4$ subdomains, $n_p = 5$ ports, $P(1) = \{1, 3\}$, $P(2) = \{1, 2\}$, $P(3) = \{2, 4\}$, $P(4) = \{3, 4\}$, $P(5) = \{1, 2, 3, 4\}$; and $Q(1) = \{1, 2, 5\}$, $Q(2) = \{2, 3, 5\}$, $Q(3) = \{1, 4, 5\}$, $Q(4) = \{3, 4, 5\}$. Ports P_1, P_2, P_3, P_4 are two-component ports, and port P_5 is four-component port. (See Appendix A.2 for more details about corner nodes.)

p_i -dimensional trial subspace with $p_i = p_i^\Omega + p_i^\Gamma$ as $\mathbf{x}_i \approx \tilde{\mathbf{x}}_i \equiv (\tilde{\mathbf{x}}_i^\Omega, \tilde{\mathbf{x}}_i^\Gamma) = (\Phi_i^\Omega \hat{\mathbf{x}}_i^\Omega, \Phi_i^\Gamma \hat{\mathbf{x}}_i^\Gamma) \in \text{Ran}(\Phi_i^\Omega) \times \text{Ran}(\Phi_i^\Gamma) \subseteq \mathbb{R}^{n_i^\Omega} \times \mathbb{R}^{n_i^\Gamma}$.

We formulate the domain-decomposition LSPG (DD-LSPG) reduced-order model by minimizing the sum of squared residual norms over these trial subspaces subject to (possibly weak) port-compatibility conditions, i.e., we compute $(\hat{\mathbf{x}}_i^\Omega, \hat{\mathbf{x}}_i^\Gamma)$, $i = 1, \dots, n_\Omega$ as the solution to the optimization problem

$$\begin{aligned}
 & \underset{(\hat{\mathbf{w}}_i^\Omega, \hat{\mathbf{w}}_i^\Gamma), i=1, \dots, n_\Omega}{\text{minimize}} && \frac{1}{2} \sum_{i=1}^{n_\Omega} \|\mathbf{B}_i \mathbf{r}_i(\Phi_i^\Omega \hat{\mathbf{w}}_i^\Omega, \Phi_i^\Gamma \hat{\mathbf{w}}_i^\Gamma)\|_2^2 \\
 & \text{subject to} && \sum_{i=1}^{n_\Omega} \mathbf{A}_i \Phi_i^\Gamma \hat{\mathbf{w}}_i^\Gamma = \mathbf{0}.
 \end{aligned} \tag{3.1}$$

Here, $\mathbf{A}_i \in \mathbb{R}^{n_A \times n_i^\Gamma}$, $i = 1, \dots, n_\Omega$ denote constraint matrices (see Section 3.3 for how this can be derived from the constraint matrices $\tilde{\mathbf{A}}_i$, $i = 1, \dots, n_\Omega$) with $n_A \leq n_{\tilde{\mathbf{A}}}$ denotes the number of constraints incurred by port compatibility, and $\mathbf{B}_i \in \mathbb{R}^{n_i^\beta \times n_i^\Gamma}$, $i = 1, \dots, n_\Omega$ with $n_i^\beta \leq n_i^\Gamma$ denotes a matrix that enables the subdomain residuals to be minimized in any weighted ℓ^2 -(semi)norm.

In particular, we focus on three choices of matrix \mathbf{B}_i : $\mathbf{B}_i = \mathbf{I}$ as in “standard” LSPG, $\mathbf{B}_i = \mathbf{Z}_i$ in the case of collocation hyper-reduction [32, 39, 40], and $\mathbf{B}_i = (\mathbf{Z}_i \Phi_i^\Gamma)^\dagger \mathbf{Z}_i$ in the case of gappy POD hyper-reduction [33, 37, 41] (see Appendix A for more details). Here, $\mathbf{Z}_i := [e_{\xi_i^1} \dots e_{\xi_i^{n_i^\Gamma}}]^T \in \{0, 1\}^{n_i^\beta \times n_i^\Gamma}$ comprises selected

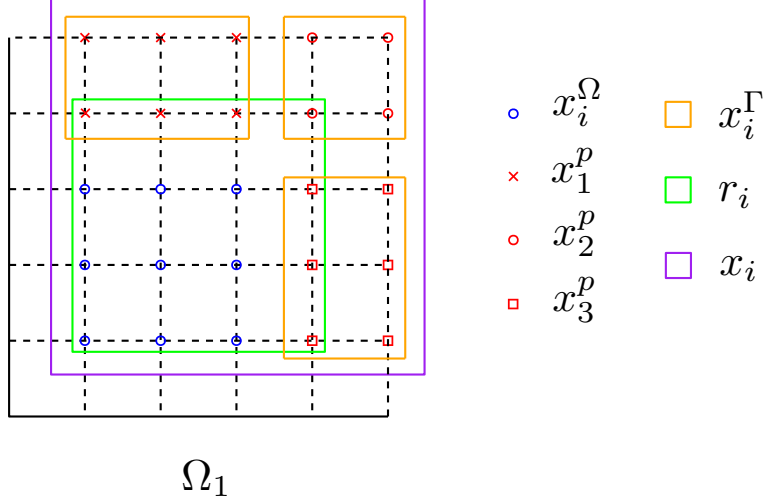


Figure 2: Domain-decomposition example: full-order model derived from discretizing a PDE in two spatial dimensions using a residual operator with a 9-point stencil. This figure considers the bottom-left subdomain Ω_1 of Fig. 1: interior DOFs (blue circles), interface DOFs (nodes included in yellow rectangle), residual DOFs (nodes included in green rectangle) and subdomain DOFs (nodes included in purple rectangle). The remaining boundary nodes correspond to given specified boundary conditions.

rows of the $n_i^r \times n_i^r$ identity matrix, \mathbf{e}_i denotes the i th Kronecker vector, and $\{\xi_i^1, \dots, \xi_i^{n_i^z}\} \subseteq \{1, \dots, n_i^r\}$ denotes the indices of the residual elements sampled by the operator. On the other hand, $\Phi_i^r \in \mathbb{R}_*^{n_i^r \times p_i^r}$, $i = 1, \dots, n_\Omega$ denote reduced bases for the residual and the superscript $+$ denotes the Moore–Penrose pseudoinverse. For the pseudoinverses to correspond to left inverses, the matrices $\mathbf{Z}_i \Phi_i^r$, $i = 1, \dots, n_\Omega$ must have full column rank, which in turn necessitates $n_i^z \geq p_i^r$, $i = 1, \dots, n_\Omega$. Note that $n_i^B = n_i^z$ for collocation hyper-reduction and $n_i^B = p_i^r$ in the case of gappy POD hyper-reduction. We note that hyper-reduction is required to ensure that computing the ROM solution incurs an n -independent operation count.

3.2 Full-subdomain bases

We also consider a variation on this formulation corresponding to the case of classical full-subdomain reduced bases [1, 3, 22, 27]. In this case, each subdomain is equipped with a single reduced basis $\Phi_i \in \mathbb{R}_*^{n_i \times p_i}$ whose columns can have support over both interior and interface degrees of freedom such that $\Phi_i^\Omega = \mathbf{P}_i^\Omega \Phi_i \in \mathbb{R}^{n_i^\Omega \times p_i^\Omega}$ and $\Phi_i^\Gamma = \mathbf{P}_i^\Gamma \Phi_i \in \mathbb{R}^{n_i^\Gamma \times p_i^\Gamma}$ with $p_i^\Omega = p_i^\Gamma = p_i$; note that the reduced bases Φ_i^Ω and Φ_i^Γ need not have full column rank individually. Approximating the solution on the i th subdomain as $\mathbf{x}_i \approx \tilde{\mathbf{x}}_i \equiv (\tilde{\mathbf{x}}_i^\Omega, \tilde{\mathbf{x}}_i^\Gamma) = (\Phi_i^\Omega \hat{\mathbf{x}}_i, \Phi_i^\Gamma \hat{\mathbf{x}}_i)$, the resulting DD-LSPG model computes solutions $\hat{\mathbf{x}}_i$, $i = 1, \dots, n_\Omega$ as the solution to the optimization problem

$$\begin{aligned}
 & \underset{\hat{\mathbf{w}}_i, i=1, \dots, n_\Omega}{\text{minimize}} && \frac{1}{2} \sum_{i=1}^{n_\Omega} \|\mathbf{B}_i \mathbf{r}_i(\Phi_i^\Omega \hat{\mathbf{w}}_i, \Phi_i^\Gamma \hat{\mathbf{w}}_i)\|_2^2 \\
 & \text{subject to} && \sum_{i=1}^{n_\Omega} \mathbf{A}_i \Phi_i^\Gamma \hat{\mathbf{w}}_i = \mathbf{0}.
 \end{aligned} \tag{3.2}$$

We again consider the choices of $\mathbf{B}_i = \mathbf{I}$, $\mathbf{B}_i = \mathbf{Z}_i$, and $\mathbf{B}_i = (\mathbf{Z}_i \Phi_i^r)^+ \mathbf{Z}_i$.

For both Problems (3.1) and (3.2), the effective number of degrees of freedom in the resulting ROM corresponds to $p = \sum_{i=1}^{n_\Omega} p_i - \text{rank}(\mathbf{A})$. Here, we have defined the reduced constraint matrix as $\mathbf{A} := [\mathbf{A}_1 \Phi_1^\Gamma \cdots \mathbf{A}_{n_\Omega} \Phi_{n_\Omega}^\Gamma]$. This result holds because the null space of the operator \mathbf{A} defines the effective subspace over which unconstrained minimization takes place.

3.3 Strong versus weak compatibility constraints

Recall that the constraint matrices $\bar{\mathbf{A}}_i$, $i = 1, \dots, n_\Omega$ are derived by enforcing the degrees of freedom on each port to be consistent across shared subdomains according to Eq. (3.3). We can effectively reduce the number of constraints by weakening this notion of consistency through enforcing a zero inner product between the difference between port solutions and a collection of prescribed test functions, i.e.,

$$\mathbf{C}^j \mathbf{P}_i^j \mathbf{x}_i^\Gamma = \mathbf{C}^j \mathbf{P}_\ell^j \mathbf{x}_\ell^\Gamma, \quad i, \ell \in P(j), \quad j = 1, \dots, n_p, \quad (3.3)$$

where $\mathbf{C}^j \in \mathbb{R}^{n_j^c \times n_j^p}$ with $n_j^c \leq n_j^p$ and $\text{rank}(\mathbf{C}^j) = n_j^c$ denotes the matrix of test functions. If we assemble a constraint matrix from (weak) compatibility conditions (3.3) in the same manner that the original constraint matrices $\bar{\mathbf{A}}_i$, $i = 1, \dots, n_\Omega$ were assembled from (strong) compatibility conditions (3.3), we obtain the constraint matrices $\mathbf{A}_i \in \mathbb{R}^{n_A \times n_i^\Gamma}$, $i = 1, \dots, n_\Omega$ with $n_A = \sum_{j=1}^{n_p} n_j^{\text{pair}} n_j^c$ that have the structure $\mathbf{A}_i = \mathbf{C} \bar{\mathbf{A}}_i$ for some $\mathbf{C} \in \mathbb{R}^{n_A \times n_{\bar{\mathbf{A}}}}$, with $\mathbf{C} = \mathbf{I}$ in the case of strong compatibility constraints (3.3). We generate \mathbf{C}^j from normal distribution, e.g., using *randn* function in MATLAB. This matrix is widely used to sample from large data and obtain optimal averaging effect. For example, randomized SVD introduced in [42] uses exactly the same random matrix. Our numerical examples show that this choice is effective.

Remark 1. *Critically, the case of weak compatibility constraints (i.e., $n_j^c < n_j^p$) admits discrepancies between the restrictions of subdomain solutions to the j th port, i.e., Eq. (3.3) will not hold in general. This phenomenon precludes the existence of a ‘global solution’, as ports may not have a uniquely computed solution. While this may appear to be deleterious to the accuracy of the computed DD-LSPG solution, we show in the numerical experiments that this relaxation is critical to obtain accurate solutions when neighboring components have incompatible bases on the associated port; this occurs in particular for interface and full-subdomain bases. For such bases, enforcing strong compatibility constraints effectively causes the subdomains to generate the trivial solution on the associated ports, yielding poor overall solution accuracy, even if the solution on the ports is uniquely defined. In summary, the existence of a solution depends heavily on the compatibility of the port bases. If the incompatible port bases are generated, then a weak constraint is necessary for the existence of a solution. On the other hand, if the compatible port bases are used, then both strong and weak constraints ensure the existence of a solution.*

4 Sequential quadratic programming solver

Problems (3.1)–(3.2) can be classified as a *nonlinear least-squares problems with linear equality constraints*. As such, they are well-suited to solution with a sequential quadratic programming (SQP) method, which in this case is equivalent to applying Newton’s method to the Karush–Kuhn–Tucker (KKT) necessary conditions for optimality. This section describes this solution approach.

4.1 Interior/boundary bases

We begin by defining the Lagrangian associated with problem (3.1)

$$L : (\hat{\mathbf{w}}_1^\Omega, \hat{\mathbf{w}}_1^\Gamma, \dots, \hat{\mathbf{w}}_{n_\Omega}^\Omega, \hat{\mathbf{w}}_{n_\Omega}^\Gamma, \gamma) \mapsto \frac{1}{2} \sum_{i=1}^{n_\Omega} \|\mathbf{B}_i \mathbf{r}_i(\Phi_i^\Omega \hat{\mathbf{w}}_i^\Omega, \Phi_i^\Gamma \hat{\mathbf{w}}_i^\Gamma)\|_2^2 + \sum_{i=1}^{n_\Omega} \gamma^T \mathbf{A}_i \Phi_i^\Gamma \hat{\mathbf{w}}_i^\Gamma, \quad (4.1)$$

where $\gamma \in \mathbb{R}^{n_A}$ denotes Lagrange multipliers. The KKT conditions arise from stationarity of the Lagrangian, i.e., the DD-LSPG ROM solution $(\hat{\mathbf{x}}_1^\Omega, \hat{\mathbf{x}}_1^\Gamma, \dots, \hat{\mathbf{x}}_{n_\Omega}^\Omega, \hat{\mathbf{x}}_{n_\Omega}^\Gamma, \boldsymbol{\lambda})$ satisfies

$$\begin{aligned} \frac{\partial L}{\partial \hat{\mathbf{w}}_i^\Omega}(\hat{\mathbf{x}}_1^\Omega, \hat{\mathbf{x}}_1^\Gamma, \dots, \hat{\mathbf{x}}_{n_\Omega}^\Omega, \hat{\mathbf{x}}_{n_\Omega}^\Gamma, \boldsymbol{\lambda}) &= \hat{\mathbf{r}}_i^\Omega(\hat{\mathbf{x}}_i^\Omega, \hat{\mathbf{x}}_i^\Gamma) = \mathbf{0}, \quad i = 1, \dots, n_\Omega \\ \frac{\partial L}{\partial \hat{\mathbf{w}}_i^\Gamma}(\hat{\mathbf{x}}_1^\Omega, \hat{\mathbf{x}}_1^\Gamma, \dots, \hat{\mathbf{x}}_{n_\Omega}^\Omega, \hat{\mathbf{x}}_{n_\Omega}^\Gamma, \boldsymbol{\lambda}) &= \hat{\mathbf{r}}_i^\Gamma(\hat{\mathbf{x}}_i^\Omega, \hat{\mathbf{x}}_i^\Gamma, \boldsymbol{\lambda}) = \mathbf{0}, \quad i = 1, \dots, n_\Omega \\ \frac{\partial L}{\partial \boldsymbol{\gamma}}(\hat{\mathbf{x}}_1^\Omega, \hat{\mathbf{x}}_1^\Gamma, \dots, \hat{\mathbf{x}}_{n_\Omega}^\Omega, \hat{\mathbf{x}}_{n_\Omega}^\Gamma, \boldsymbol{\lambda}) &= \sum_{i=1}^{n_\Omega} \mathbf{A}_i \boldsymbol{\Phi}_i^\Gamma \hat{\mathbf{x}}_i^\Gamma = \mathbf{0}, \end{aligned} \quad (4.2)$$

where we have defined

$$\begin{aligned} \hat{\mathbf{r}}_i^\Omega : (\hat{\mathbf{w}}_i^\Omega, \hat{\mathbf{w}}_i^\Gamma) &\mapsto [\boldsymbol{\Phi}_i^\Omega]^T \frac{\partial \mathbf{r}_i}{\partial \hat{\mathbf{x}}_i^\Omega}(\boldsymbol{\Phi}_i^\Omega \hat{\mathbf{w}}_i^\Omega, \boldsymbol{\Phi}_i^\Gamma \hat{\mathbf{w}}_i^\Gamma)^T [\mathbf{B}_i]^T \mathbf{B}_i \mathbf{r}_i(\boldsymbol{\Phi}_i^\Omega \hat{\mathbf{w}}_i^\Omega, \boldsymbol{\Phi}_i^\Gamma \hat{\mathbf{w}}_i^\Gamma) \\ \hat{\mathbf{r}}_i^\Gamma : (\hat{\mathbf{w}}_i^\Omega, \hat{\mathbf{w}}_i^\Gamma, \boldsymbol{\gamma}) &\mapsto [\boldsymbol{\Phi}_i^\Gamma]^T \frac{\partial \mathbf{r}_i}{\partial \hat{\mathbf{x}}_i^\Gamma}(\boldsymbol{\Phi}_i^\Omega \hat{\mathbf{w}}_i^\Omega, \boldsymbol{\Phi}_i^\Gamma \hat{\mathbf{w}}_i^\Gamma)^T [\mathbf{B}_i]^T \mathbf{B}_i \mathbf{r}_i(\boldsymbol{\Phi}_i^\Omega \hat{\mathbf{w}}_i^\Omega, \boldsymbol{\Phi}_i^\Gamma \hat{\mathbf{w}}_i^\Gamma) + [\boldsymbol{\Phi}_i^\Gamma]^T \mathbf{A}_i^T \boldsymbol{\gamma} \end{aligned} \quad (4.3)$$

for $i = 1, \dots, n_\Omega$. Applying Newton's method with a Gauss-Newton Hessian approximation to solve the system of nonlinear algebraic equations (4.2) yields the SQP iterations for $k = 0, \dots, K$

$$\begin{bmatrix} \mathbf{H}_1^{\Omega\Omega}(\hat{\mathbf{x}}_1^{\Omega(k)}, \hat{\mathbf{x}}_1^{\Gamma(k)}) & \mathbf{H}_1^{\Omega\Gamma}(\hat{\mathbf{x}}_1^{\Omega(k)}, \hat{\mathbf{x}}_1^{\Gamma(k)}) & \dots & \mathbf{0} & \mathbf{0} & \mathbf{0} \\ \mathbf{H}_1^{\Gamma\Omega}(\hat{\mathbf{x}}_1^{\Omega(k)}, \hat{\mathbf{x}}_1^{\Gamma(k)}) & \mathbf{H}_1^{\Gamma\Gamma}(\hat{\mathbf{x}}_1^{\Omega(k)}, \hat{\mathbf{x}}_1^{\Gamma(k)}) & \dots & \mathbf{0} & \mathbf{0} & [\boldsymbol{\Phi}_1^\Gamma]^T \mathbf{A}_1^T \\ \vdots & \vdots & \ddots & \vdots & \vdots & \vdots \\ \mathbf{0} & \mathbf{0} & \dots & \mathbf{H}_{n_\Omega}^{\Omega\Omega}(\hat{\mathbf{x}}_{n_\Omega}^{\Omega(k)}, \hat{\mathbf{x}}_{n_\Omega}^{\Gamma(k)}) & \mathbf{H}_{n_\Omega}^{\Omega\Gamma}(\hat{\mathbf{x}}_{n_\Omega}^{\Omega(k)}, \hat{\mathbf{x}}_{n_\Omega}^{\Gamma(k)}) & \mathbf{0} \\ \mathbf{0} & \mathbf{0} & \dots & \mathbf{H}_{n_\Omega}^{\Gamma\Omega}(\hat{\mathbf{x}}_{n_\Omega}^{\Omega(k)}, \hat{\mathbf{x}}_{n_\Omega}^{\Gamma(k)}) & \mathbf{H}_{n_\Omega}^{\Gamma\Gamma}(\hat{\mathbf{x}}_{n_\Omega}^{\Omega(k)}, \hat{\mathbf{x}}_{n_\Omega}^{\Gamma(k)}) & [\boldsymbol{\Phi}_{n_\Omega}^\Gamma]^T \mathbf{A}_{n_\Omega}^T \\ \mathbf{0} & \mathbf{A}_1 \boldsymbol{\Phi}_1^\Gamma & \dots & \mathbf{0} & \mathbf{A}_{n_\Omega} \boldsymbol{\Phi}_{n_\Omega}^\Gamma & \mathbf{0} \end{bmatrix} \begin{bmatrix} \mathbf{p}_1^{\Omega(k)} \\ \mathbf{p}_1^{\Gamma(k)} \\ \vdots \\ \mathbf{p}_{n_\Omega}^{\Omega(k)} \\ \mathbf{p}_{n_\Omega}^{\Gamma(k)} \\ \mathbf{p}^{\boldsymbol{\lambda}(k)} \end{bmatrix} = \begin{bmatrix} \hat{\mathbf{r}}_1^\Omega(\hat{\mathbf{x}}_1^{\Omega(k)}, \hat{\mathbf{x}}_1^{\Gamma(k)}) \\ \hat{\mathbf{r}}_1^\Gamma(\hat{\mathbf{x}}_1^{\Omega(k)}, \hat{\mathbf{x}}_1^{\Gamma(k)}) \\ \vdots \\ \hat{\mathbf{r}}_{n_\Omega}^\Omega(\hat{\mathbf{x}}_{n_\Omega}^{\Omega(k)}, \hat{\mathbf{x}}_{n_\Omega}^{\Gamma(k)}) \\ \hat{\mathbf{r}}_{n_\Omega}^\Gamma(\hat{\mathbf{x}}_{n_\Omega}^{\Omega(k)}, \hat{\mathbf{x}}_{n_\Omega}^{\Gamma(k)}) \\ \sum_{i=1}^{n_\Omega} \mathbf{A}_i \boldsymbol{\Phi}_i^\Gamma \hat{\mathbf{x}}_i^\Gamma \end{bmatrix} \quad (4.4)$$

where

$$\begin{aligned} \mathbf{H}_i^{\Omega\Omega} : (\hat{\mathbf{w}}_i^\Omega, \hat{\mathbf{w}}_i^\Gamma) &\mapsto [\boldsymbol{\Phi}_i^\Omega]^T \frac{\partial \mathbf{r}_i}{\partial \hat{\mathbf{w}}_i^\Omega}(\boldsymbol{\Phi}_i^\Omega \hat{\mathbf{w}}_i^\Omega, \boldsymbol{\Phi}_i^\Gamma \hat{\mathbf{w}}_i^\Gamma)^T [\mathbf{B}_i]^T \mathbf{B}_i \frac{\partial \mathbf{r}_i}{\partial \hat{\mathbf{w}}_i^\Omega}(\boldsymbol{\Phi}_i^\Omega \hat{\mathbf{w}}_i^\Omega, \boldsymbol{\Phi}_i^\Gamma \hat{\mathbf{w}}_i^\Gamma) \boldsymbol{\Phi}_i^\Omega \\ \mathbf{H}_i^{\Omega\Gamma} : (\hat{\mathbf{w}}_i^\Omega, \hat{\mathbf{w}}_i^\Gamma) &\mapsto [\boldsymbol{\Phi}_i^\Omega]^T \frac{\partial \mathbf{r}_i}{\partial \hat{\mathbf{w}}_i^\Omega}(\boldsymbol{\Phi}_i^\Omega \hat{\mathbf{w}}_i^\Omega, \boldsymbol{\Phi}_i^\Gamma \hat{\mathbf{w}}_i^\Gamma)^T [\mathbf{B}_i]^T \mathbf{B}_i \frac{\partial \mathbf{r}_i}{\partial \hat{\mathbf{w}}_i^\Gamma}(\boldsymbol{\Phi}_i^\Omega \hat{\mathbf{w}}_i^\Omega, \boldsymbol{\Phi}_i^\Gamma \hat{\mathbf{w}}_i^\Gamma) \boldsymbol{\Phi}_i^\Gamma \\ \mathbf{H}_i^{\Gamma\Omega} : (\hat{\mathbf{w}}_i^\Omega, \hat{\mathbf{w}}_i^\Gamma) &\mapsto [\boldsymbol{\Phi}_i^\Gamma]^T \frac{\partial \mathbf{r}_i}{\partial \hat{\mathbf{w}}_i^\Gamma}(\boldsymbol{\Phi}_i^\Omega \hat{\mathbf{w}}_i^\Omega, \boldsymbol{\Phi}_i^\Gamma \hat{\mathbf{w}}_i^\Gamma)^T [\mathbf{B}_i]^T \mathbf{B}_i \frac{\partial \mathbf{r}_i}{\partial \hat{\mathbf{w}}_i^\Omega}(\boldsymbol{\Phi}_i^\Omega \hat{\mathbf{w}}_i^\Omega, \boldsymbol{\Phi}_i^\Gamma \hat{\mathbf{w}}_i^\Gamma) \boldsymbol{\Phi}_i^\Omega \\ \mathbf{H}_i^{\Gamma\Gamma} : (\hat{\mathbf{w}}_i^\Omega, \hat{\mathbf{w}}_i^\Gamma) &\mapsto [\boldsymbol{\Phi}_i^\Gamma]^T \frac{\partial \mathbf{r}_i}{\partial \hat{\mathbf{w}}_i^\Gamma}(\boldsymbol{\Phi}_i^\Omega \hat{\mathbf{w}}_i^\Omega, \boldsymbol{\Phi}_i^\Gamma \hat{\mathbf{w}}_i^\Gamma)^T [\mathbf{B}_i]^T \mathbf{B}_i \frac{\partial \mathbf{r}_i}{\partial \hat{\mathbf{w}}_i^\Gamma}(\boldsymbol{\Phi}_i^\Omega \hat{\mathbf{w}}_i^\Omega, \boldsymbol{\Phi}_i^\Gamma \hat{\mathbf{w}}_i^\Gamma) \boldsymbol{\Phi}_i^\Gamma \end{aligned} \quad (4.5)$$

for $i = 1, \dots, n_\Omega$. We can then update the solution as

$$\begin{aligned} \hat{\mathbf{x}}_i^{\Omega(k+1)} &= \hat{\mathbf{x}}_i^{\Omega(k)} + \alpha^{(k)} \mathbf{p}_i^{\Omega(k)}, \quad i = 1, \dots, n_\Omega \\ \hat{\mathbf{x}}_i^{\Gamma(k+1)} &= \hat{\mathbf{x}}_i^{\Gamma(k)} + \alpha^{(k)} \mathbf{p}_i^{\Gamma(k)}, \quad i = 1, \dots, n_\Omega \\ \boldsymbol{\lambda}^{(k+1)} &= \boldsymbol{\lambda}^{(k)} + \alpha^{(k)} \mathbf{p}^{\boldsymbol{\lambda}(k)}, \end{aligned} \quad (4.6)$$

where $\alpha^{(k)}$ is a step length that can be computed, e.g., via line search. We note that the sparse block structure of SQP iterations (4.4) admit interesting parallel-solution strategies, which is the subject of future work. We also note that the Gauss–Newton approximation is widely used for the solution process of nonlinear problems due to its practicality, i.e., no need to compute an exact Hessian and often achieve a quadratic convergence rate although its convergence is not guaranteed [43]. Our numerical examples show that the Gauss–Newton method works well for the problems considered in this paper.

4.2 Full-subdomain bases

Analogously to Section 4.1, the Lagrangian associated with problem (3.2) is defined as

$$L : (\hat{\mathbf{w}}_1, \dots, \hat{\mathbf{w}}_{n_\Omega}, \boldsymbol{\gamma}) \mapsto \frac{1}{2} \sum_{i=1}^{n_\Omega} \|\mathbf{B}_i \mathbf{r}_i(\boldsymbol{\Phi}_i^\Omega \hat{\mathbf{w}}_i, \boldsymbol{\Phi}_i^\Gamma \hat{\mathbf{w}}_i)\|_2^2 + \sum_{i=1}^{n_\Omega} \boldsymbol{\gamma}^T \mathbf{A}_i \boldsymbol{\Phi}_i^\Gamma \hat{\mathbf{w}}_i, \quad (4.7)$$

where the KKT system can be derived from stationarity of the Lagrangian such that the DD-LSPG ROM solution $(\hat{\mathbf{x}}_1, \dots, \hat{\mathbf{x}}_{n_\Omega}, \boldsymbol{\lambda})$ satisfies

$$\begin{aligned} \frac{\partial L}{\partial \hat{\mathbf{w}}_i}(\hat{\mathbf{x}}_1, \dots, \hat{\mathbf{x}}_{n_\Omega}, \boldsymbol{\lambda}) &= \hat{\mathbf{r}}_i(\hat{\mathbf{x}}_i, \boldsymbol{\lambda}) = \mathbf{0}, \quad i = 1, \dots, n_\Omega \\ \frac{\partial L}{\partial \boldsymbol{\lambda}}(\hat{\mathbf{x}}_1, \dots, \hat{\mathbf{x}}_{n_\Omega}, \boldsymbol{\lambda}) &= \sum_{i=1}^{n_\Omega} \mathbf{A}_i \boldsymbol{\Phi}_i^\Gamma \hat{\mathbf{x}}_i = \mathbf{0}, \end{aligned} \quad (4.8)$$

where we have defined

$$\begin{aligned} \hat{\mathbf{r}}_i : (\hat{\mathbf{w}}_i, \boldsymbol{\gamma}) \mapsto & [\boldsymbol{\Phi}_i^\Omega]^T \frac{\partial \mathbf{r}_i}{\partial \mathbf{w}_i^\Omega}(\boldsymbol{\Phi}_i^\Omega \hat{\mathbf{w}}_i, \boldsymbol{\Phi}_i^\Gamma \hat{\mathbf{w}}_i)^T [\mathbf{B}_i]^T \mathbf{B}_i \mathbf{r}_i(\boldsymbol{\Phi}_i^\Omega \hat{\mathbf{w}}_i, \boldsymbol{\Phi}_i^\Gamma \hat{\mathbf{w}}_i) \\ & + [\boldsymbol{\Phi}_i^\Gamma]^T \frac{\partial \mathbf{r}_i}{\partial \mathbf{w}_i^\Gamma}(\boldsymbol{\Phi}_i^\Omega \hat{\mathbf{x}}_i, \boldsymbol{\Phi}_i^\Gamma \hat{\mathbf{x}}_i)^T [\mathbf{B}_i]^T \mathbf{B}_i \mathbf{r}_i(\boldsymbol{\Phi}_i^\Omega \hat{\mathbf{x}}_i, \boldsymbol{\Phi}_i^\Gamma \hat{\mathbf{x}}_i) + (\boldsymbol{\Phi}_i^\Gamma)^T \mathbf{A}_i^T \boldsymbol{\gamma} \end{aligned} \quad (4.9)$$

for $i = 1, \dots, n_\Omega$. Applying Newton’s method with a Gauss–Newton Hessian approximation to solve the system of nonlinear algebraic equations (4.8) yields the SQP iterations for $k = 0, \dots, K$

$$\begin{bmatrix} \mathbf{H}_1(\hat{\mathbf{x}}_1^{(k)}) & \dots & \mathbf{0} & (\boldsymbol{\Phi}_1^\Gamma)^T \mathbf{A}_1^T \\ \vdots & \ddots & \vdots & \vdots \\ \mathbf{0} & \dots & \mathbf{H}_{n_\Omega}(\hat{\mathbf{x}}_{n_\Omega}^{(k)}) & (\boldsymbol{\Phi}_{n_\Omega}^\Gamma)^T \mathbf{A}_{n_\Omega}^T \\ \mathbf{A}_1 \boldsymbol{\Phi}_1^\Gamma & \dots & \mathbf{A}_{n_\Omega} \boldsymbol{\Phi}_{n_\Omega}^\Gamma & \mathbf{0} \end{bmatrix} \begin{bmatrix} \mathbf{p}_1^{(k)} \\ \vdots \\ \mathbf{p}_{n_\Omega}^{(k)} \\ \mathbf{p}^\lambda \end{bmatrix} = - \begin{bmatrix} \hat{\mathbf{r}}_1(\hat{\mathbf{x}}_1^{(k)}) \\ \vdots \\ \hat{\mathbf{r}}_{n_\Omega}(\hat{\mathbf{x}}_{n_\Omega}^{(k)}) \\ \sum_{i=1}^{n_\Omega} \mathbf{A}_i \boldsymbol{\Phi}_i^\Gamma \hat{\mathbf{x}}_i^{(k)} \end{bmatrix}, \quad (4.10)$$

where

$$\begin{aligned} \mathbf{H}_i : \hat{\mathbf{w}}_i \mapsto & [\boldsymbol{\Phi}_i^\Omega]^T \frac{\partial \mathbf{r}_i}{\partial \mathbf{w}_i^\Omega}(\boldsymbol{\Phi}_i^\Omega \hat{\mathbf{w}}_i, \boldsymbol{\Phi}_i^\Gamma \hat{\mathbf{w}}_i)^T [\mathbf{B}_i]^T \mathbf{B}_i \frac{\partial \mathbf{r}_i}{\partial \mathbf{w}_i^\Omega}(\boldsymbol{\Phi}_i^\Omega \hat{\mathbf{w}}_i, \boldsymbol{\Phi}_i^\Gamma \hat{\mathbf{w}}_i) \boldsymbol{\Phi}_i^\Omega \\ & + [\boldsymbol{\Phi}_i^\Omega]^T \frac{\partial \mathbf{r}_i}{\partial \mathbf{w}_i^\Omega}(\boldsymbol{\Phi}_i^\Omega \hat{\mathbf{w}}_i, \boldsymbol{\Phi}_i^\Gamma \hat{\mathbf{w}}_i)^T [\mathbf{B}_i]^T \mathbf{B}_i \frac{\partial \mathbf{r}_i}{\partial \mathbf{w}_i^\Gamma}(\boldsymbol{\Phi}_i^\Omega \hat{\mathbf{w}}_i, \boldsymbol{\Phi}_i^\Gamma \hat{\mathbf{w}}_i) \boldsymbol{\Phi}_i^\Gamma \\ & + [\boldsymbol{\Phi}_i^\Gamma]^T \frac{\partial \mathbf{r}_i}{\partial \mathbf{w}_i^\Gamma}(\boldsymbol{\Phi}_i^\Omega \hat{\mathbf{w}}_i, \boldsymbol{\Phi}_i^\Gamma \hat{\mathbf{w}}_i)^T [\mathbf{B}_i]^T \mathbf{B}_i \frac{\partial \mathbf{r}_i}{\partial \mathbf{w}_i^\Omega}(\boldsymbol{\Phi}_i^\Omega \hat{\mathbf{w}}_i, \boldsymbol{\Phi}_i^\Gamma \hat{\mathbf{w}}_i) \boldsymbol{\Phi}_i^\Omega \\ & + [\boldsymbol{\Phi}_i^\Gamma]^T \frac{\partial \mathbf{r}_i}{\partial \mathbf{w}_i^\Gamma}(\boldsymbol{\Phi}_i^\Omega \hat{\mathbf{w}}_i, \boldsymbol{\Phi}_i^\Gamma \hat{\mathbf{w}}_i)^T [\mathbf{B}_i]^T \mathbf{B}_i \frac{\partial \mathbf{r}_i}{\partial \mathbf{w}_i^\Gamma}(\boldsymbol{\Phi}_i^\Omega \hat{\mathbf{w}}_i, \boldsymbol{\Phi}_i^\Gamma \hat{\mathbf{w}}_i) \boldsymbol{\Phi}_i^\Gamma \end{aligned} \quad (4.11)$$

for $i = 1, \dots, n_\Omega$. We can then update the solution as

$$\begin{aligned} \hat{\mathbf{x}}_i^{(k+1)} &= \hat{\mathbf{x}}_i^{(k)} + \alpha^{(k)} \mathbf{p}_i^{(k)}, \quad i = 1, \dots, n_\Omega \\ \boldsymbol{\lambda}^{(k+1)} &= \boldsymbol{\lambda}^{(k)} + \alpha^{(k)} \mathbf{p}^\lambda, \end{aligned} \quad (4.12)$$

where $\alpha^{(k)}$ is a step length that can be computed, e.g., via line search.

5 Online algorithm and computational cost

We now describe the computational cost of executing the online stage. To make this precise, we first introduce the sampling operators $\mathbf{Z}_i^r \in \{0, 1\}^{n_i^{z,r} \times n_i}$, $\mathbf{Z}_i^\Omega \in \{0, 1\}^{n_i^{z,\Omega} \times n_i^\Omega}$, and $\mathbf{Z}_i^\Gamma \in \{0, 1\}^{n_i^{z,\Gamma} \times n_i^\Gamma}$, $i = 1, \dots, n_\Omega$, which comprise selected rows of the $n_i \times n_i$, $n_i^\Omega \times n_i^\Omega$, and $n_i^\Gamma \times n_i^\Gamma$ identity matrices, respectively. These matrices are those of the prescribed structure that satisfy

$$\mathbf{B}_i[\mathbf{Z}_i^r]^T \mathbf{Z}_i^r \mathbf{r}_i([\mathbf{Z}_i^\Omega]^T \mathbf{Z}_i^\Omega \mathbf{w}_i^\Omega, [\mathbf{Z}_i^\Gamma]^T \mathbf{Z}_i^\Gamma \mathbf{w}_i^\Gamma) = \mathbf{B}_i \mathbf{r}_i(\mathbf{w}_i^\Omega, \mathbf{w}_i^\Gamma), \quad \forall \mathbf{w}_i^\Omega \in \mathbb{R}^{n_i^\Omega}, \mathbf{w}_i^\Gamma \in \mathbb{R}^{n_i^\Gamma}, \quad (5.1)$$

with the fewest number of rows. In particular, \mathbf{Z}_i^Ω and \mathbf{Z}_i^Γ sample the degrees of freedom associated with nonzero columns of the Jacobians $\mathbf{B}_i \frac{\partial \mathbf{r}_i}{\partial \mathbf{w}_i^\Omega}$ and $\mathbf{B}_i \frac{\partial \mathbf{r}_i}{\partial \mathbf{w}_i^\Gamma}$, respectively.

Note that for standard LSPG (i.e., $\mathbf{B}_i = \mathbf{I}$), we have simply $\mathbf{Z}_i^r = \mathbf{I}$, $\mathbf{Z}_i^\Omega = \mathbf{I}$, and $\mathbf{Z}_i^\Gamma = \mathbf{I}$ with $n_i^{z,r} = n_i$, $n_i^{z,\Omega} = n_i^\Omega$, and $n_i^{z,\Gamma} = n_i^\Gamma$. For collocation (i.e., $\mathbf{B}_i = \mathbf{Z}_i$) and gappy POD (i.e., $\mathbf{B}_i = (\mathbf{Z}_i \Phi_i^r)^+ \mathbf{Z}_i$), we have $\mathbf{Z}_i^r = \mathbf{Z}_i$, $n_i^{z,r} = n_i^z$, $n_i^{z,\Omega} \ll n_i^\Omega$ and $n_i^{z,\Gamma} \ll n_i^\Gamma$ if $n_i^z \ll n_i$ and the Jacobians $\frac{\partial \mathbf{r}_i}{\partial \mathbf{w}_i^\Omega}$ and $\frac{\partial \mathbf{r}_i}{\partial \mathbf{w}_i^\Gamma}$ are sparse.

Algorithms 1 and 2 describe the assembly and solve steps required within each SQP iteration, respectively, while Tables 1 and 2 report the associated floating-point operation counts.

Algorithm 1 and Table 1 show that Steps 1–3 of the online assembly can be parallelized across the subdomains, while Step 4 requires a reduction across subdomains. Further, these illuminate that $n_i^{z,\Omega}$, $n_i^{z,\Gamma}$, $n_i^{z,r} \ll n_i$ are necessary in order to achieve an n -independent online operation count; this is precisely what is provided by hyper-reduction. Here, c_i^r and c_i^J denote the average number of floating point operations required to evaluate one entry of the i th residual and one row of the i th Jacobian matrix, respectively, while w_i^Ω and w_i^Γ denote the average number of non-zeros per row of the i th Jacobian for the interior and interface, respectively. Note that the operation counts for assembly are identical for the interior/boundary bases and full-subdomain bases cases.

Algorithm 2 and Table 2 report the steps and associated computational costs associated with the solve and update for each SQP iteration. Importantly, we see that the online solve and update depend only on the dimensions of the reduced bases and constraint matrices; as such, they are independent of the quantities $n_i^{z,\Omega}$, $n_i^{z,\Gamma}$, and $n_i^{z,r}$ and are thus unaffected by hyper-reduction. Also, here we observe noticeable differences in the operation counts associated with the interior/boundary bases and full-subdomain bases cases. In the case of interior/boundary bases, using a specialized Cholesky-based LDL^T factorization [44], the solve cost for system (4.4) is $\frac{1}{3}(s_{dM})^3$ with system dimension $s_{dM} = \sum_{i=1}^{n_\Omega} p_i^\Omega + \sum_{i=1}^{n_\Omega} p_i^\Gamma + n_A$ ⁴. In contrast, in the case of full-subdomain bases, the solve cost for system (4.10) is $\frac{1}{3}(s_{dM}^s)^3$ with dimension system $s_{dM}^s = n_\Omega p_i + n_A$. Thus, we expect the solve cost to be less expensive for the full-subdomain cases when similar reduced-basis dimensions are employed.

Algorithm 1: Interior/boundary bases: Online assembly at each SQP iteration

1: **Parallel:** Compute the required elements of the state

$$(\mathbf{Z}_i^\Omega \tilde{\mathbf{x}}_i^{\Omega(k)}, \mathbf{Z}_i^\Gamma \tilde{\mathbf{x}}_i^{\Gamma(k)}) = (\mathbf{Z}_i^\Omega \Phi_i^\Omega \hat{\mathbf{x}}_i^{\Omega(k)}, \mathbf{Z}_i^\Gamma \Phi_i^\Gamma \hat{\mathbf{x}}_i^{\Gamma(k)}) \text{ for } i = 1, \dots, n_\Omega;$$

2: **Parallel:** Compute residual $\mathbf{B}_i \mathbf{r}_i(\mathbf{Z}_i^\Omega \tilde{\mathbf{x}}_i^{\Omega(k)}, \mathbf{Z}_i^\Gamma \tilde{\mathbf{x}}_i^{\Gamma(k)})$, Jacobians $\mathbf{B}_i \frac{\partial \mathbf{r}_i}{\partial \mathbf{w}_i^\Omega}(\mathbf{Z}_i^\Omega \tilde{\mathbf{x}}_i^{\Omega(k)}, \mathbf{Z}_i^\Gamma \tilde{\mathbf{x}}_i^{\Gamma(k)}) \Phi_i^\Omega$,

$$\mathbf{B}_i \frac{\partial \mathbf{r}_i}{\partial \mathbf{w}_i^\Gamma}(\mathbf{Z}_i^\Omega \tilde{\mathbf{x}}_i^{\Omega(k)}, \mathbf{Z}_i^\Gamma \tilde{\mathbf{x}}_i^{\Gamma(k)}) \Phi_i^\Gamma, \text{ constraint } \mathbf{A}_i \Phi_i^\Gamma \hat{\mathbf{x}}_i^\Gamma, \text{ and } [\Phi_i^\Gamma]^T [\mathbf{A}_i]^T \boldsymbol{\lambda}^{(k)} \text{ for } i = 1, \dots, n_\Omega;$$

3: **Parallel:** Using these quantities, compute terms that appear in the SQP system;

- **Interior/boundary bases:** compute $\hat{\mathbf{r}}_i^\Omega(\hat{\mathbf{x}}_i^{\Omega(k)}, \hat{\mathbf{x}}_i^{\Gamma(k)})$, $\hat{\mathbf{r}}_i^\Gamma(\hat{\mathbf{x}}_i^{\Omega(k)}, \hat{\mathbf{x}}_i^{\Gamma(k)})$, $\boldsymbol{\lambda}^{(k)}$, $\mathbf{H}_i^{\Omega\Omega}(\hat{\mathbf{x}}_i^{\Omega(k)}, \hat{\mathbf{x}}_i^{\Gamma(k)})$, $\mathbf{H}_i^{\Omega\Gamma}(\hat{\mathbf{x}}_i^{\Omega(k)}, \hat{\mathbf{x}}_i^{\Gamma(k)})$, $\mathbf{H}_i^{\Gamma\Omega}(\hat{\mathbf{x}}_i^{\Omega(k)}, \hat{\mathbf{x}}_i^{\Gamma(k)})$, and $\mathbf{H}_i^{\Gamma\Gamma}(\hat{\mathbf{x}}_i^{\Omega(k)}, \hat{\mathbf{x}}_i^{\Gamma(k)})$ for $i = 1, \dots, n_\Omega$.

- **Full-subdomain basis:** compute $\hat{\mathbf{r}}_i(\hat{\mathbf{x}}_i^{\Omega(k)}, \hat{\mathbf{x}}_i^{\Gamma(k)})$, $\mathbf{H}_i(\hat{\mathbf{x}}_i^{\Omega(k)}, \hat{\mathbf{x}}_i^{\Gamma(k)})$, for $i = 1, \dots, n_\Omega$;

4: **Serial:** Reduce constraints over subdomains $\sum_{i=1}^{n_\Omega} \mathbf{A}_i \Phi_i^\Gamma \hat{\mathbf{x}}_i^\Gamma$;

⁴For reference, a better solver based on antitriangular factorization for saddle point matrices that was proposed recently [45, 46] has the solving cost of only $8mn^2 - 2m^2(n + m/3)$ flops where $n = \sum_{i=1}^{n_\Omega} (p_i^\Omega + p_i^\Gamma)$ and $m = n_A$.

Algorithm 2: Interior/boundary bases: Online solve and update at each SQP iteration

- 5: **Serial:** Solve the SQP system (4.4) or (4.10);
6: **Serial:** Update the boundary and interface states via Eq. (4.6) or (4.12);
7: **Serial:** Update the Lagrange multipliers via Eq. (4.6) or (4.12);
-

Table 1: Algorithm 1 operation count

Algorithm 1 step	Parallel/serial	Floating point operation count
1	Parallel	$2n_i^{z,\Omega} p_i^\Omega + 2n_i^{z,\Gamma} p_i^\Gamma$ for the i th subdomain
2	Parallel	$n_i^{z,r} c_i^r + n_i^{z,r} c_i^l + 2n_i^{z,r} w_i^\Omega p_i^\Omega + 2n_i^{z,r} w_i^\Gamma p_i^\Gamma + 4n_A p_i^\Gamma + \mathbf{is_dense}(\mathbf{B}_i) (2n_i^B n_i^{z,r} (1 + p_i^\Omega + p_i^\Gamma))$ for the i th subdomain
3	Parallel	$2p_i^\Omega n_i^B + 2p_i^\Gamma n_i^B + p_i^\Gamma + (n_i^B)^2 \left((p_i^\Gamma)^2 + 2p_i^\Gamma p_i^\Omega + (p_i^\Omega)^2 \right)$ for the i th subdomain
4	Serial	$2n_\Omega n_A$

Table 2: Algorithm 2 operation count

Algorithm 2 step	Parallel/serial	Floating point operation count
5	Serial	Interior/boundary bases: $\frac{1}{3} (n_\Omega p_i^\Omega + n_\Omega p_i^\Gamma + n_A)^3$ Full-subdomain bases: $\frac{1}{3} (n_\Omega p_i + n_A)^3$
6	Serial	$2n_\Omega (p_i^\Omega + p_i^\Gamma)$ for the i th subdomain
7	Serial	$2n_A$

6 Basis construction

This section describes how the different proposed reduced bases can be constructed assuming that a full-system state-snapshot matrix $\mathbf{X} := [\mathbf{x}(\boldsymbol{\mu}_{\text{train}}^1) \cdots \mathbf{x}(\boldsymbol{\mu}_{\text{train}}^{n_{\text{train}}})] \in \mathbb{R}^{n \times n_{\text{train}}}$ with $\{\boldsymbol{\mu}_{\text{train}}^j\}_{j=1}^{n_{\text{train}}} \subseteq \mathcal{D}$ has been precomputed during an “offline” training stage. Section 8.1.6 describes a specific approach to construct the snapshots from subdomain/component training snapshots alone, which will be necessary for truly extreme-scale models and decomposable systems. Algorithm 3 lists the widely-used proper orthogonal decomposition (POD) algorithm that we employ to construct all proposed reduced bases in this work. Throughout, $v \in [0, 1]$ is the “energy criterion” used to determine the applied truncation.

Algorithm 3: POD: Proper orthogonal decomposition

Input: Snapshots $\mathbf{X} \in \mathbb{R}^{n \times m}$, energy criterion $v \in [0, 1]$

Output: Reduced-basis matrix $\Phi \in \mathbb{R}^{n \times p}$

- 1: Compute (thin) singular value decomposition: $\mathbf{X} = \mathbf{U} \boldsymbol{\Sigma} \mathbf{V}^T$,
 - 2: Set $\Phi = [\mathbf{u}_1 \cdots \mathbf{u}_p]$, where $p = \min_{i \in \Gamma(v)}$, $\Gamma(v) := \{i \mid \sum_{j=1}^i \sigma_j / \sum_{k=1}^m \sigma_k \geq 1 - v\}$. Here, $\mathbf{U} \equiv [\mathbf{u}_1 \cdots \mathbf{u}_m]$ and $\boldsymbol{\Sigma} \equiv \text{diag}(\sigma_1, \dots, \sigma_m)$.
-

6.1 Interior/boundary bases

We first describe various approaches to constructing interior/boundary bases.

- **Interior bases.** To compute interior bases $\Phi_i^\Omega \in \mathbb{R}_{\star}^{n_i^\Omega \times p_i^\Omega}$, $i = 1, \dots, n_\Omega$, we simply execute Algorithm 3 with snapshots isolated to subdomain interiors such that $\Phi_i^\Omega = \text{POD}(\mathbf{P}_i^\Omega \mathbf{X}, v)$, $i = 1, \dots, n_\Omega$.
- **(Boundary) Full-interface bases.** Analogously, we compute full-interface bases by executing Algorithm 3 with snapshots isolated to subdomain interfaces such that $\Phi_i^\Gamma = \text{POD}(\mathbf{P}_i^\Gamma \mathbf{X}, v)$, $i = 1, \dots, n_\Omega$.
- **(Boundary) Port bases.** To compute port bases, we first compute reduced bases for each port by executing Algorithm 3 with snapshots $\mathbf{P}_\ell^j \mathbf{P}_\ell^\Gamma \mathbf{X}$, $j = 1, \dots, n_p$ with any $\ell \in P(j)$, and compute the resulting interface bases by assembling the appropriate port bases as $\Phi_i^\Gamma = [\text{POD}(\mathbf{P}_i^{q_i^1} \mathbf{P}_i^\Gamma \mathbf{X}, v) \cdots \text{POD}(\mathbf{P}_i^{q_i^{|Q(i)|}} \mathbf{P}_i^\Gamma \mathbf{X}, v)]$, $i = 1, \dots, n_\Omega$, where $Q(i) \equiv \{q_i^j\}_j$.
- **(Boundary) Skeleton bases.** This approach first computes a reduced basis for the “skeleton”, which is the union of subdomain interfaces, and subsequently isolates that basis to each subdomain’s interface while ensuring full column rank on that interface. More precisely, we compute $\bar{\Phi}_i^\Gamma = \text{POD}((\mathbf{I} - \sum_{i=1}^{n_\Omega} [\mathbf{P}_i^\Omega]^T \mathbf{P}_i^\Omega) \mathbf{X}, v)$ followed by a rank-revealing QR factorization with column pivoting $\bar{\Phi}_i^\Gamma \mathbf{P} = \mathbf{Q}_i \mathbf{R}_i$, and finally set $\Phi_i^\Gamma = [\mathbf{q}_i^1 \cdots \mathbf{q}_i^{p_i^\Gamma}]$, where $\mathbf{Q}_i \equiv [\mathbf{q}_i^1 \cdots \mathbf{q}_i^{n_{\text{train}}}]$ and $\text{rank}(\bar{\Phi}_i^\Gamma) = p_i^\Gamma (\leq n_{\text{train}})$. We note that skeleton bases require full-system snapshots and thus are not generally practical for either extreme-scale systems nor for decomposable systems, as both of these scenarios in practice preclude the ability to collect full-system snapshots; nevertheless, because this work does not directly consider subsystem/component-based training, we include this approach in the present work.

6.2 Full-subdomain basis

The full-subdomain-basis approach computes reduced bases that have support over all degrees of freedom for their respective subdomains, and subsequently isolates this basis to the subdomain interior and interface.

That is, we compute $\Phi_i = \text{POD}\left(\begin{bmatrix} \mathbf{P}_i^\Omega \\ \mathbf{P}_i^\Gamma \end{bmatrix} \mathbf{X}, v\right)$ and set $\Phi_i^\Omega = [\mathbf{I}_{n_i^\Omega} \quad \mathbf{0}_{n_i^\Omega}] \Phi_i$ and $\Phi_i^\Gamma = [\mathbf{0}_{n_i^\Omega \times n_i^\Gamma} \quad \mathbf{I}_{n_i^\Gamma \times n_i^\Gamma}] \Phi_i$, where \mathbf{I}_n and $\mathbf{0}_n$ denote the $n \times n$ identity and zero matrices, respectively.

7 *A posteriori* and *a priori* error bounds

For notational simplicity, this section omits explicit parameter dependence; results can be interpreted as holding for any arbitrary parameter instance $\boldsymbol{\mu} \in \mathcal{D}$. We begin by stating assumptions that will be employed in subsequent analysis.

A1 The DD-LSPG ROM employs strong constraints, i.e., $\mathbf{A}_i = \bar{\mathbf{A}}_i$, $i = 1, \dots, n_\Omega$.

Under Assumption A1, the DD-LSPG ROMs can be converted to unconstrained minimization problems. First, we introduce the null-space matrix $\bar{\mathbf{N}} \in \mathbb{R}^{\sum_{i=1}^{n_\Omega} p_i^\Gamma \times p^{\text{null}}}$ with $p^{\text{null}} := \sum_{i=1}^{n_\Omega} p_i^\Gamma - \text{rank}(\bar{\mathbf{A}})$, which satisfies $\bar{\mathbf{A}} \bar{\mathbf{N}} = \mathbf{0}$ with $\bar{\mathbf{A}} := [\bar{\mathbf{A}}_1 \Phi_1^\Gamma \cdots \bar{\mathbf{A}}_{n_\Omega} \Phi_{n_\Omega}^\Gamma]$. Because strong constraints enforce a global solution such that Eq. (3.3) holds (e.g., see Remark 1), DD-LSPG yields a ‘global’ solution $\tilde{\mathbf{x}} \in \mathbb{R}^n$ satisfying

$$\tilde{\mathbf{x}}_i^\Omega = \mathbf{P}_i^\Omega \tilde{\mathbf{x}}, \quad \tilde{\mathbf{x}}_i^\Gamma = \mathbf{P}_i^\Gamma \tilde{\mathbf{x}}, \quad i = 1, \dots, n_\Omega. \quad (7.1)$$

Now, the interior/boundary-basis problem (3.1) is equivalent to the unconstrained minimization problem wherein $\hat{\mathbf{x}}_i^\Omega$, $i = 1, \dots, n_\Omega$ and $\hat{\mathbf{x}}^{\text{null}}$ comprise the solution to the problem

$$\underset{(\hat{\mathbf{w}}_i^\Omega)_{i=1, \dots, n_\Omega}, \hat{\mathbf{w}}^{\text{null}}}{\text{minimize}} \quad \frac{1}{2} \sum_{i=1}^{n_\Omega} \|\mathbf{B}_i \mathbf{r}_i(\Phi_i^\Omega \hat{\mathbf{w}}_i^\Omega, \Phi_i^\Gamma \bar{\mathbf{N}}_i \hat{\mathbf{w}}^{\text{null}})\|_2^2, \quad (7.2)$$

with

$$\mathbf{x}_i \approx \tilde{\mathbf{x}}_i \equiv (\tilde{\mathbf{x}}_i^\Omega, \tilde{\mathbf{x}}_i^\Gamma) = (\Phi_i^\Omega \hat{\mathbf{x}}_i^\Omega, \Phi_i^\Gamma \bar{N}_i \hat{\mathbf{x}}^{\text{null}}), \quad (7.3)$$

where $\bar{N}_i \in \mathbb{R}^{p_i^\Gamma \times p^{\text{null}}}$ denotes the i th row block of \bar{N} .

Note that Problem (7.2) can be expressed equivalently as computing $\tilde{\mathbf{x}}$ that satisfies

$$\underset{\mathbf{w} \in \mathcal{S}_{I/B}}{\text{minimize}} \quad \frac{1}{2} \sum_{i=1}^{n_\Omega} \|\mathbf{B}_i \mathbf{r}_i(\mathbf{P}_i^\Omega \mathbf{w}, \mathbf{P}_i^\Gamma \mathbf{w})\|_2^2, \quad (7.4)$$

where the trial subspace $\mathcal{S}_{I/B} \subseteq \mathbb{R}^n$ is defined as

$$\begin{aligned} \mathcal{S}_{I/B} := & \{\mathbf{w} \in \mathbb{R}^n \mid \exists \hat{\mathbf{w}}_i^\Omega \in \mathbb{R}^{p_i^\Omega}, i = 1, \dots, n_\Omega, \text{ and } \hat{\mathbf{w}}^{\text{null}} \in \mathbb{R}^{p^{\text{null}}} \text{ s.t.} \\ & \mathbf{P}_i^\Omega \mathbf{w} = \Phi_i^\Omega \hat{\mathbf{w}}_i^\Omega, \mathbf{P}_i^\Gamma \mathbf{w} = \Phi_i^\Gamma \bar{N}_i \hat{\mathbf{w}}^{\text{null}}, i = 1, \dots, n_\Omega\} \subseteq \mathbb{R}^n. \end{aligned} \quad (7.5)$$

Similarly, A1 admits conversion of the full-subdomain-basis problem (3.2) to an unconstrained minimization problem wherein $\hat{\mathbf{x}}^{\text{null}}$ comprises the solution to the problem

$$\underset{\hat{\mathbf{w}}^{\text{null}}}{\text{minimize}} \quad \frac{1}{2} \sum_{i=1}^{n_\Omega} \|\mathbf{B}_i \mathbf{r}_i(\Phi_i^\Omega \bar{N}_i \hat{\mathbf{w}}^{\text{null}}, \Phi_i^\Gamma \bar{N}_i \hat{\mathbf{w}}^{\text{null}})\|_2^2. \quad (7.6)$$

with

$$\mathbf{x}_i \approx \tilde{\mathbf{x}}_i \equiv (\tilde{\mathbf{x}}_i^\Omega, \tilde{\mathbf{x}}_i^\Gamma) = (\Phi_i^\Omega \bar{N}_i \hat{\mathbf{x}}^{\text{null}}, \Phi_i^\Gamma \bar{N}_i \hat{\mathbf{x}}^{\text{null}}), \quad (7.7)$$

which can be expressed equivalently as computing $\tilde{\mathbf{x}}$ that satisfies

$$\underset{\mathbf{w} \in \mathcal{S}_F}{\text{minimize}} \quad \frac{1}{2} \sum_{i=1}^{n_\Omega} \|\mathbf{B}_i \mathbf{r}_i(\mathbf{P}_i^\Omega \mathbf{w}, \mathbf{P}_i^\Gamma \mathbf{w})\|_2^2, \quad (7.8)$$

where the trial subspace $\mathcal{S}_F \subseteq \mathbb{R}^n$ is defined as

$$\mathcal{S}_F := \{\mathbf{w} \in \mathbb{R}^n \mid \exists \hat{\mathbf{w}}^{\text{null}} \in \mathbb{R}^{p^{\text{null}}} \text{ s.t. } \mathbf{P}_i^\Omega \mathbf{w} = \Phi_i^\Omega \bar{N}_i \hat{\mathbf{w}}^{\text{null}}, \mathbf{P}_i^\Gamma \mathbf{w} = \Phi_i^\Gamma \bar{N}_i \hat{\mathbf{w}}^{\text{null}}, i = 1, \dots, n_\Omega\} \subseteq \mathbb{R}^n, \quad (7.9)$$

We now introduce two more assumptions needed for the error bounds.

A2 The residual is inverse Lipschitz continuous in the ℓ^2 -norm, i.e., there exists $\kappa_\ell > 0$ such that

$$\left(\sum_{i=1}^{n_\Omega} \|\mathbf{r}_i(\mathbf{w}_i^\Omega, \mathbf{w}_i^\Gamma) - \mathbf{r}_i(\mathbf{y}_i^\Omega, \mathbf{y}_i^\Gamma)\|_2^2 \right)^{1/2} \geq \kappa_\ell \|\mathbf{w} - \mathbf{y}\|_2, \quad \forall \mathbf{w}, \mathbf{y} \in \mathbb{R}^n \quad (7.10)$$

with $\mathbf{w}_i^\Omega := \mathbf{Z}_i^\Omega \mathbf{w}$, $\mathbf{w}_i^\Gamma := \mathbf{Z}_i^\Gamma \mathbf{w}$, $\mathbf{y}_i^\Omega := \mathbf{Z}_i^\Omega \mathbf{y}$, and $\mathbf{y}_i^\Gamma := \mathbf{Z}_i^\Gamma \mathbf{y}$, $i = 1, \dots, n_\Omega$.

A3 The $\mathbf{B}^T \mathbf{B}$ -norm and the ℓ^2 -norm of the residual are equivalent over all elements of the trial subspace such that there exists $P > 0$ such that

$$\left(\sum_{i=1}^{n_\Omega} \|\mathbf{B}_i \mathbf{r}_i(\mathbf{P}_i^\Omega \mathbf{w}, \mathbf{P}_i^\Gamma \mathbf{w})\|_2^2 \right)^{1/2} \geq P \left(\sum_{i=1}^{n_\Omega} \|\mathbf{r}_i(\mathbf{P}_i^\Omega \mathbf{w}, \mathbf{P}_i^\Gamma \mathbf{w})\|_2^2 \right)^{1/2}, \quad \forall \mathbf{w} \in \mathcal{S} \subseteq \mathbb{R}^n, \quad (7.11)$$

where $\mathcal{S} = \mathcal{S}_{I/B}$ in the case of interior/boundary bases and $\mathcal{S} = \mathcal{S}_F$ in the case of full-domain bases.

Proposition 1 (*A posteriori* error bound). *Under Assumptions A1–A3, the error in the DD-LSPG ROM approximate solution for both interior/boundary bases and full-subdomain bases can be bounded as*

$$\max\left(\max_{i \in \{1, \dots, n_\Omega\}} \|\mathbf{x}_i^\Omega - \tilde{\mathbf{x}}_i^\Omega\|_2, \max_{j \in \{1, \dots, n_p\}} \|\mathbf{P}^j \mathbf{x} - \mathbf{P}^j \tilde{\mathbf{x}}\|_2 \right) \leq \|\mathbf{x} - \tilde{\mathbf{x}}\|_2 \leq \frac{1}{P \kappa_\ell} \left(\sum_{i=1}^{n_\Omega} \|\mathbf{B}_i \mathbf{r}_i(\tilde{\mathbf{x}}_i^\Omega, \tilde{\mathbf{x}}_i^\Gamma)\|_2^2 \right)^{1/2}, \quad (7.12)$$

where $\tilde{\mathbf{x}} \in \mathbb{R}^n$ is the ‘global’ solution satisfying Eq. (7.1) and where $\mathbf{P}^j \in \{0, 1\}^{n_j \times n}$, $j = 1, \dots, n_p$ comprises selected rows of the identity matrix that extract the global degrees of freedom associated with the j th port.

Proof. Leveraging the norm-equivalence relation $\|\cdot\|_\infty \leq \|\cdot\|_2$, the ‘global’ solution relations (7.1), sequentially invoking A2 and A3, and noting that $\mathbf{r}_i(\mathbf{x}_i^\Omega, \mathbf{x}_i^\Gamma) = 0$, $i = 1, \dots, n_\Omega$ yields

$$\max_{i \in \{1, \dots, n_\Omega\}} \|\mathbf{x}_i^\Omega - \tilde{\mathbf{x}}_i^\Omega\|_2 \leq \|\mathbf{x} - \tilde{\mathbf{x}}\|_2 \leq \frac{1}{\kappa_\ell} \left(\sum_{i=1}^{n_\Omega} \|\mathbf{r}_i(\tilde{\mathbf{x}}_i^\Omega, \tilde{\mathbf{x}}_i^\Gamma)\|_2^2 \right)^{1/2} \leq \frac{1}{P\kappa_\ell} \left(\sum_{i=1}^{n_\Omega} \|\mathbf{B}_i \mathbf{r}_i(\tilde{\mathbf{x}}_i^\Omega, \tilde{\mathbf{x}}_i^\Gamma)\|_2^2 \right)^{1/2}, \quad (7.13)$$

which is valid for both interior/boundary bases and full-subdomain bases according to A3. On the invocation of the ℓ^∞ -norm, we have decomposed the state vector into segments: one for each group of interior degrees of freedom, and one for each port. \square

We now introduce another assumption that will be employed to derive *a priori* error bounds.

A4 The residual is Lipschitz continuous in the $\mathbf{B}^T \mathbf{B}$ -norm, i.e., there exists $\kappa_u > 0$ such that

$$\left(\sum_{i=1}^{n_\Omega} \|\mathbf{B}_i \mathbf{r}_i(\mathbf{w}_i^\Omega, \mathbf{w}_i^\Gamma) - \mathbf{B}_i \mathbf{r}_i(\mathbf{y}_i^\Omega, \mathbf{y}_i^\Gamma)\|_2^2 \right)^{1/2} \leq \kappa_u \|\mathbf{w} - \mathbf{y}\|_2, \quad \forall \mathbf{w}, \mathbf{y} \in \mathbb{R}^n. \quad (7.14)$$

Proposition 2 (*A priori* error bound with respect to the ℓ^2 -optimal approximation error). *Under Assumptions A1–A4, the error in the DD-LSPG ROM approximate solution for both interior/boundary bases and full-subdomain bases can be bounded in terms of the ℓ^2 -optimal approximation error as*

$$\|\mathbf{x} - \tilde{\mathbf{x}}\|_2 \leq \frac{\kappa_u}{P\kappa_\ell} \min_{\mathbf{w} \in \mathcal{S}} \|\mathbf{x} - \mathbf{w}\|_2 \quad (7.15)$$

where $\mathcal{S} = \mathcal{S}_{I/B}$ in the case of interior/boundary bases and $\mathcal{S} = \mathcal{S}_F$ in the case of full-subdomain bases.

Proof. We have from Eq. (7.3), and Problems (7.4) and (7.8), and Inequality (7.12) that

$$\begin{aligned} \frac{1}{P\kappa_\ell} \left(\sum_{i=1}^{n_\Omega} \|\mathbf{B}_i \mathbf{r}_i(\tilde{\mathbf{x}}_i^\Omega, \tilde{\mathbf{x}}_i^\Gamma)\|_2^2 \right)^{1/2} &= \frac{1}{P\kappa_\ell} \min_{\mathbf{w} \in \mathcal{S}} \left(\sum_{i=1}^{n_\Omega} \|\mathbf{B}_i \mathbf{r}_i(\mathbf{P}_i^\Omega \mathbf{w}, \mathbf{P}_i^\Gamma \mathbf{w})\|_2^2 \right)^{1/2} \\ &\leq \frac{1}{P\kappa_\ell} \left(\sum_{i=1}^{n_\Omega} \|\mathbf{B}_i \mathbf{r}_i(\mathbf{P}_i^\Omega \mathbf{x}^{*,2}, \mathbf{P}_i^\Gamma \mathbf{x}^{*,2})\|_2^2 \right)^{1/2} \leq \frac{\kappa_u}{P\kappa_\ell} \|\mathbf{x} - \mathbf{x}^{*,2}\|_2. \end{aligned} \quad (7.16)$$

Defining $\mathbf{x}^{*,2} := \arg \min_{\mathbf{w} \in \mathcal{S}} \|\mathbf{x} - \mathbf{w}\|_2$ and combining this with Proposition 1 yields the desired result. \square

Proposition 3 (*A priori* error bound with respect to the ℓ^∞ -optimal approximation error over subdomains). *Under Assumptions A1–A4,*

$$\begin{aligned} &\max\left(\max_{i \in \{1, \dots, n_\Omega\}} \|\mathbf{x}_i^\Omega - \tilde{\mathbf{x}}_i^\Omega\|_2, \max_{j \in \{1, \dots, n_p\}} \|\mathbf{P}^j \mathbf{x} - \mathbf{P}^j \tilde{\mathbf{x}}\|_2 \right) \\ &\leq \frac{\kappa_u \sqrt{n_\Omega + n_p}}{P\kappa_\ell} \min_{\mathbf{w} \in \mathcal{S}} \max\left(\max_{i \in \{1, \dots, n_\Omega\}} \|\mathbf{x}_i^\Omega - \mathbf{w}_i^\Omega\|_2, \max_{j \in \{1, \dots, n_p\}} \|\mathbf{P}^j \mathbf{x} - \mathbf{P}^j \mathbf{w}\|_2 \right), \end{aligned} \quad (7.17)$$

where $\mathcal{S} = \mathcal{S}_{I/B}$ in the case of interior/boundary bases and $\mathcal{S} = \mathcal{S}_F$ in the case of full-subdomain bases.

Proof. Analogously to the proof of Proposition 2 we have from Eq. (7.3), and Problems (7.4) and (7.8), and Inequality (7.12) that

$$\begin{aligned} \frac{1}{P\kappa_\ell} \left(\sum_{i=1}^{n_\Omega} \|\mathbf{B}_i \mathbf{r}_i(\tilde{\mathbf{x}}_i^\Omega, \tilde{\mathbf{x}}_i^\Gamma)\|_2^2 \right)^{1/2} &= \frac{1}{P\kappa_\ell} \min_{\mathbf{w} \in \mathcal{S}} \left(\sum_{i=1}^{n_\Omega} \|\mathbf{B}_i \mathbf{r}_i(\mathbf{P}_i^\Omega \mathbf{w}, \mathbf{P}_i^\Gamma \mathbf{w})\|_2^2 \right)^{1/2} \\ &\leq \frac{1}{P\kappa_\ell} \left(\sum_{i=1}^{n_\Omega} \|\mathbf{B}_i \mathbf{r}_i(\mathbf{P}_i^\Omega \mathbf{x}^{*,\infty}, \mathbf{P}_i^\Gamma \mathbf{x}^{*,\infty})\|_2^2 \right)^{1/2} \leq \frac{\kappa_u}{P\kappa_\ell} \|\mathbf{x} - \mathbf{x}^{*,\infty}\|_2 \\ &\leq \frac{\kappa_u \sqrt{n_\Omega + n_p}}{P\kappa_\ell} \max\left(\max_{i \in \{1, \dots, n_\Omega\}} \|\mathbf{x}_i^\Omega - \mathbf{x}_i^{\Omega,*,\infty}\|_2, \max_{j \in \{1, \dots, n_p\}} \|\mathbf{P}^j \mathbf{x} - \mathbf{P}^j \mathbf{x}^{*,\infty}\|_2 \right) \end{aligned} \quad (7.18)$$

where, on the invocation of the ℓ^∞ -norm, we have decomposed the state vector into segments: one for each group of interior degrees of freedom, and one for each port. Defining $\mathbf{x}^{*,\infty}$ as satisfying the minimization problem

$$\mathbf{x}^{*,\infty} \in \operatorname{argmin}_{\mathbf{w} \in \mathcal{S}} \max \left(\max_{i \in \{1, \dots, n_\Omega\}} \|\mathbf{x}_i^\Omega - \mathbf{w}_i^\Omega\|_2, \max_{j \in \{1, \dots, n_p\}} \|\mathbf{P}^j \mathbf{x} - \mathbf{P}^j \mathbf{w}\|_2 \right) \quad (7.19)$$

and combining with Proposition 1 yields the desired result. \square

8 Numerical experiments

This section reports numerical experiments that assess the performance of the proposed DD-LSPG method on two benchmark problems. We do not attempt to demonstrate our methods in either extreme-scale or decomposable problems. Instead, we focus on the performance of our algorithm on small problems in order to investigate the effect of some key model parameters, such as constraint type, basis type, hyper-reduction, truncation levels, on accuracy and speed in both weak and strong scaling.

We compare the following methods:

- **FOM.** This model corresponds to the full-order model, i.e., the solution satisfying Eq. (2.1) (equiv. Eq. (2.5)).
- **DD-LSPG.** This model corresponds to the unweighted LSPG ROM, i.e., the solution satisfies (3.1)–(3.2) with $\mathbf{B}_i = \mathbf{I}$, $i = 1, \dots, n_\Omega$.
- **DD-GNAT.** This model corresponds to the GNAT ROM, i.e., the solution satisfying (3.1)–(3.2) with $\mathbf{B}_i = (\mathbf{Z}_i \Phi_i^r)^+ \mathbf{Z}_i$, $i = 1, \dots, n_\Omega$. Algorithm 4 is used to construct the sampling matrices \mathbf{Z}_i , $i = 1, \dots, n_\Omega$.

We assess the accuracy of any ROM solution $\tilde{\mathbf{x}}(\boldsymbol{\mu})$ as follows

$$\text{relative error} = \sqrt{\frac{1}{n_\Omega} \sum_{i=1}^{n_\Omega} \frac{\|\tilde{\mathbf{x}}_i(\boldsymbol{\mu}) - \mathbf{x}_i(\boldsymbol{\mu})\|_2^2}{\|\mathbf{x}_i(\boldsymbol{\mu})\|_2^2}}, \quad (8.1)$$

and we measure its computational cost in terms of the wall time incurred by the ROM simulation relative to that incurred by the FOM simulation; the speedup is the reciprocal of the relative wall time. All timings are obtained by performing calculations in Matlab R2018b on an 2x6-Core Intel Xeon 2.93GHz with 64 GB RAM of memory. Reported timings comprise the average over five simulations.

8.1 Parameterized heat equation

8.1.1 Global finite-element discretization

Table 3: Heat equation, parameters of global FOM discretization

	“Coarse” mesh	“Fine” mesh
Number of elements	1600	6400
Number of nodes	1681	6561
Number of degrees of freedom n	1521	6241

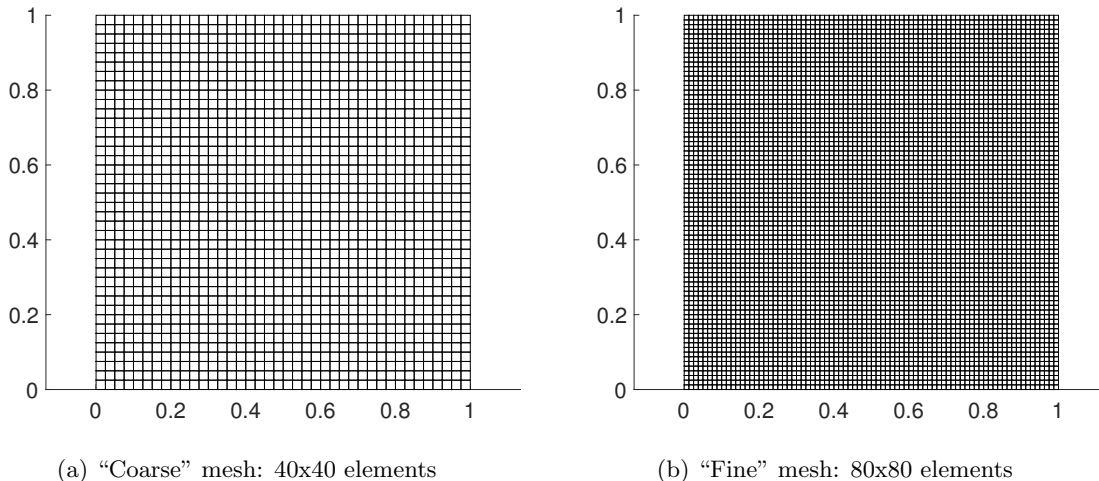


Figure 3: Heat equation, two global meshes used for discretization.

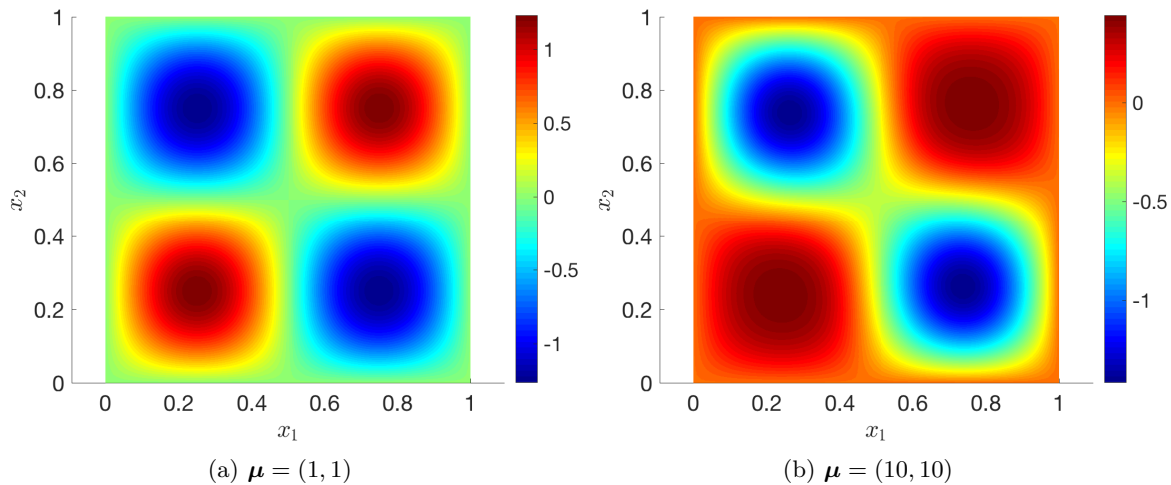


Figure 4: Heat equation, FOM solutions for different μ using the fine mesh.

We first consider the model example introduced in Refs. [47, 26]. This is a parametric nonlinear 2D heat problem which consists of computing $u(\mathbf{x}, \boldsymbol{\mu})$ with $\mathbf{x} \equiv (x_1, x_2) \in \Omega = [0, 1]^2$ and $\boldsymbol{\mu} \equiv (\mu_1, \mu_2) \in \mathcal{D} = [0.01, 10]^2$ and homogeneous Dirichlet boundary condition on $\Gamma \equiv \partial\Omega$ satisfying

$$-\nabla^2 u + \frac{\mu_1}{\mu_2} (e^{\mu_2 u} - 1) = 100 \sin(2\pi x_1) \sin(2\pi x_2). \quad (8.2)$$

This model can be interpreted as a 2D stationary diffusion problem with a nonlinear interior heat source. The resulting solution exhibits a strongly nonlinear dependence on the parameters $\boldsymbol{\mu}$.

For spatial discretization, we apply the finite-element method using two meshes (which will be used to assess strong and weak scaling): a “coarse” mesh and a “fine” mesh, characterized by 1600 (40×40) and 6400 (80×80) bilinear quadrilateral (Q1) elements, respectively. Figure 3 depicts these meshes, while Table 3 reports the corresponding parameters. Figure 4 plots the FOM reference solutions on the “fine” mesh with two different parameter values $\boldsymbol{\mu} = (1, 1)$ and $\boldsymbol{\mu} = (10, 10)$. Applying these finite-element discretizations to Eq. (8.2) leads to a parameterized system of nonlinear algebraic equations of the form (2.1).

8.1.2 Full-order model

Table 4: Heat equation, parameters for three FOM configurations

	2×2 “coarse”	4×4 “fine”	2×2 “fine”
Number of subdomains n_Ω	4	16	4
Number of constraints $n_{\bar{A}}$	172	1092	332
Number of ports n_p	5	33	5
Number of interior DOFs n_1^Ω	441	441	1681
	weak scaling		
		strong scaling	

Table 5: Heat equation, parameters on each Ω_i of the 2×2 “fine” configuration. In this case, there are $n_p = 5$ total ports with $n_1^p = 76$, $n_2^p = 76$, $n_3^p = 78$, $n_4^p = 78$, $n_5^p = 4$.

	Ω_1	Ω_2	Ω_3	Ω_4
n_i^r	1521	1560	1560	1600
n_i^Ω	1444	1482	1482	1521
n_i^Γ	156	158	158	160
$n_i (= n_i^\Omega + n_i^\Gamma)$	1600	1640	1640	1681
Number of subdomain ports $ Q(i) $	3	3	3	3

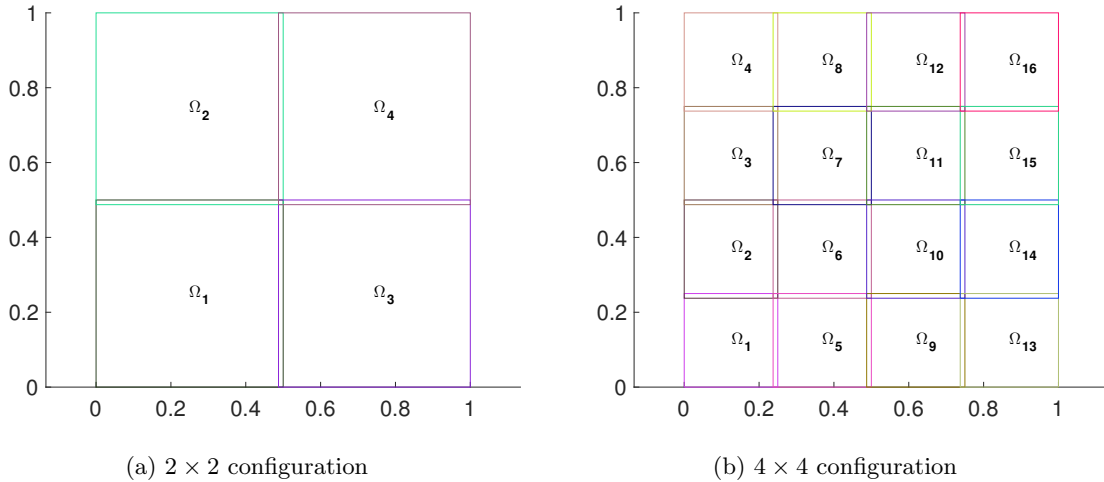


Figure 5: Heat equation, two domain decomposition configurations based on the finite-element mesh.

After applying the finite-element discretization, we introduce the algebraically non-overlapping decomposition of the problem described in Section 2. For this problem, the chosen algebraic decomposition corresponds to a spatial domain decomposition in space. In particular, we employ decompositions into both 2×2 (such that $n_\Omega = 4$) and 4×4 (such that $n_\Omega = 16$) configurations as depicted in Figure 5; note that these local subdomains have one layer of elements overlapping (as explained in Figure 1). We apply the 2×2 decomposition to the “coarse” mesh only, but apply both 4×4 and 2×2 decompositions to the “fine” mesh. Table 4 lists the parameters used for each of these configurations. The pairwise comparison of the 2×2 “coarse” and 4×4 “fine” configurations is interpreted as weak scaling, while the pairwise comparison of the

2×2 “fine” and 4×4 “fine” configurations interpreted as strong scaling, respectively. For reference, Table 5 reports the parameters characterizing each subdomain Ω_i , $i = 1, \dots, n_\Omega$ of the 2×2 “fine” configuration.

8.1.3 DD-LSPG and DD-GNAT approximations: one online computation

To generate the reduced bases required for the reduced-order models, we solve the FOM (2.1) for $\boldsymbol{\mu} \in \{\boldsymbol{\mu}_{\text{train}}^j\}_{j=1}^{n_{\text{train}}} \subset \mathcal{D}$. In our case, we define the training-parameter set $\{\boldsymbol{\mu}_{\text{train}}^j\}_{j=1}^{n_{\text{train}}}$ via a 20×20 equispaced sampling of the parameter domain \mathcal{D} , yielding $n_{\text{train}} = 400$ samples. We apply the methods described in Section 6 to create port, skeleton, full-interface, and full-subdomain bases from these training data. However, we recall that skeleton bases require full-system snapshots and thus are not generally practical for decomposable systems that demand “bottom-up” training; we still include this approach for comparative purposes. At each iteration of the Newton–Raphson algorithm used to solve the FOM equations (2.1), the residual vector is saved; the resulting residual snapshots are employed to generate the residual bases $\boldsymbol{\Phi}_i^r$, $i = 1, \dots, n_\Omega$ employed by DD-GNAT via POD. Lastly, the GNAT offline Algorithm 4 is performed to create sample meshes \boldsymbol{s}_i for all subdomains Ω_i .

Table 6: Heat equation, top-down training, 2×2 “fine” configuration, ROM methods performance at point $\boldsymbol{\mu}_{\text{test}} = (5.005, 5.005) \notin \{\boldsymbol{\mu}_{\text{train}}^j\}_{j=1}^{n_{\text{train}}}$ for one online computation. Recall from Section 6 that $v \in [0, 1]$ denotes the energy criterion employed by POD.

constraint	strong							
	port		skeleton		full-interface		subdomain	
method	DD-LSPG	DD-GNAT	DD-LSPG	DD-GNAT	DD-LSPG	DD-GNAT	DD-LSPG	DD-GNAT
v for state	$1 - 10^{-5}$	$1 - 10^{-5}$	$1 - 10^{-5}$	$1 - 10^{-5}$	$1 - 10^{-5}$	$1 - 10^{-5}$	$1 - 10^{-5}$	$1 - 10^{-5}$
v for residual		$1 - 10^{-12}$		$1 - 10^{-12}$		$1 - 10^{-12}$		$1 - 10^{-12}$
n_i^z/p_i^r		2		2		2		2
rel. error	0.0026	0.0012	0.0025	0.0019	0.6959	0.6667	1.0000	1.0000
speedup	3.87	8.86	3.88	8.82	3.91	8.85	13.61	30.98

Table 7: Heat equation, top-down training, 2×2 “fine” configuration, ROM parameters on each Ω_i resulting from Table 6.

basis	port				skeleton				full-interface				subdomain			
	Ω_1	Ω_2	Ω_3	Ω_4	Ω_1	Ω_2	Ω_3	Ω_4	Ω_1	Ω_2	Ω_3	Ω_4	Ω_1	Ω_2	Ω_3	Ω_4
n_A	18				9				12				12			
p_i^Ω	4	2	2	4	4	2	2	4	4	2	2	4	4	2	2	4
p_i^Γ	8	8	8	8	3	3	3	3	3	3	3	3	4	2	2	4
p_1^p	3	3	3	3												
p_2^p	2	2	2	2												
p_3^p	3	3	3	3												
n_i^z	102	310	310	104	102	310	310	104	102	310	310	104	102	310	310	104
p_i^r	51	155	155	52	51	155	155	52	51	155	155	52	51	155	155	52

We now compare the DD-LSPG and DD-GNAT methods for fixed values of their parameters, and for a single randomly selected online point $\boldsymbol{\mu}_{\text{test}} = (5.005, 5.005) \notin \{\boldsymbol{\mu}_{\text{train}}^j\}_{j=1}^{n_{\text{train}}}$; results at other online points are qualitatively similar. Table 6 reports the chosen input parameters and associated performance of the methods, while the resulting ROM parameters over each subdomain Ω_i , $i = 1, \dots, n_\Omega$ are listed on Table 7. The results in Table 6 confirm the comments in Remark 1, which suggested that enforcing strong compatibility can yield poor results for full-interface and full-subdomain bases, and that only port and (generally impractical) skeleton bases are well-suited for strong compatibility constraints. Figure 6 visualizes DD-LSPG

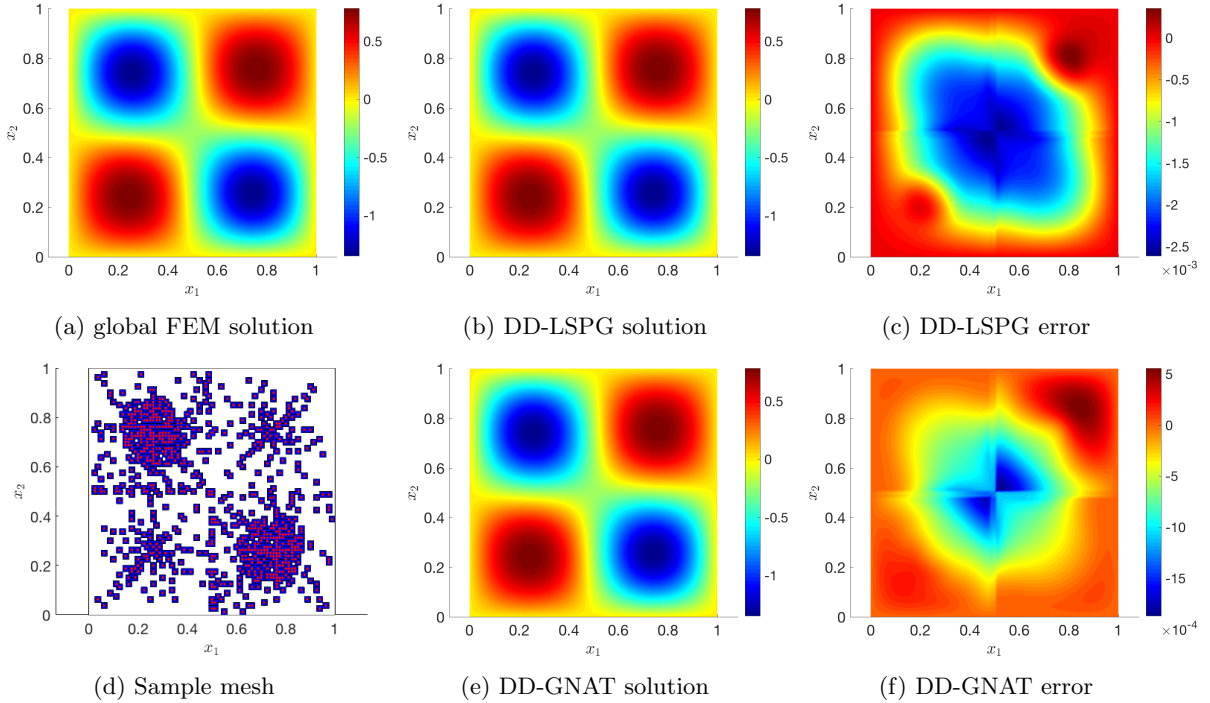


Figure 6: Heat equation, top-down training, 2×2 “fine” configuration, port bases in Table 6, solutions visualized on Ω .

and DD-GNAT solutions for the port-bases case: it shows that DD-LSPG and DD-GNAT yield accurate results for port bases with strong constraints as anticipated. Table 7 also shows specifically that p_i^r is about one order of magnitude larger than p_i , note that this is normal as $n_i^z \geq p_i^r \geq p_i$ is a necessary consistency condition to ensure the GNAT method works (see [33, 37]). Figure 6d shows that the DD-GNAT method picks many sampling points near the center region of Ω_i to capture well the solution nonlinearity and hence ensures the desired solution accuracy. As a result, the DD-GNAT method provides almost similar solution to that of DD-LSPG, hence almost similar good accuracy (see Figures 6c and 6f).

8.1.4 DD-LSPG and DD-GNAT approximations: parameter study

Because assessing a given method’s performance for a single instance of its parameters does not lend insight into the model’s complete error–cost performance tradeoff, this section subjects each of the proposed ROMs to a parameter study wherein each model parameter is varied between limits specified in Table 8. Here, we choose several *high* energy criteria for both the interior and boundary bases to obtain sufficient number of bases over all subdomains, thus ensure good solution accuracy. All other parameters are chosen straightforwardly.

For each weak compatibility constraint case, we generate five sets of random matrices \mathbf{C}^j , $j = 1, \dots, n_p$, which in turn yields five different sets of constraint matrices \mathbf{A}_i , $i = 1 \dots, n_\Omega$ as described in Section 3.3. We use each set to perform one ROM simulation, and record the associated timing and relative error of that simulation. The reported timing and relative error comprises the average obtained over these five simulations. For the strong-constraint case, we perform only one simulation as $\mathbf{A}_i = \bar{\mathbf{A}}_i$ defined uniquely. The recorded wall time for any parallel step is set to the largest wall time incurred by any subdomain, while that for any serial step is simply set to overall wall time incurred by the step (see Algorithms 1–2).

From these results, we then construct a Pareto front to characterize the error–cost for each method. This Pareto front is characterized by the collection of method–parameter instances that yield simulation results

Table 8: Heat equation, top-down training, ROM-method parameters limits for parameter study (skel.=skeleton, intf.=full-interface, subdom.=subdomain). Recall from Section 6 that $v \in [0, 1]$ denotes the energy criterion employed by POD.

method	DD-LSPG	DD-GNAT
v on Ω_i for interior/boundary bases	$\{1 - 10^{-5}, 1 - 10^{-8}\}$	$\{1 - 10^{-5}, 1 - 10^{-8}\}$
v on Γ_i for interior/boundary bases	$\{1 - 10^{-5}, 1 - 10^{-8}\}$	$\{1 - 10^{-5}, 1 - 10^{-8}\}$
v for full-subdomain bases	$\{1 - 10^{-3}, 1 - 10^{-5}, 1 - 10^{-7}, 1 - 10^{-9}\}$	$\{1 - 10^{-3}, 1 - 10^{-5}, 1 - 10^{-7}, 1 - 10^{-9}\}$
v for r_i		$\{1 - 10^{-6}, 1 - 10^{-8}, 1 - 10^{-10}, 1 - 10^{-12}\}$
n_i^z/p_i^r		$\{1, 1.5, 2, 4\}$
constraint type	$\{1, 2, 3, 4, 5, \text{strong}\}$	$\{1, 2, 3, 4, 5, \text{strong}\}$
basis types	$\{\text{port, skel., intf., subdom.}\}$	$\{\text{port, skel., intf., subdom.}\}$

that are not dominated in both relative error or wall time by any other method-parameter instance. Figure 7 reports these Pareto fronts for the three configurations considered. Figure 8 plots the average relative error versus number of constraints per port for the 4×4 “fine” configuration.

We first analyze the solve wall time, and thus consider the subfigures in the rightmost column of Figure 7. These plots yield the following observations:

- (i) For a given basis type, the solve costs for DD-LSPG and DD-GNAT are nearly the same, which is sensible because they yield SQP systems of the same dimension and structure.
- (ii) The 4×4 “fine” configuration yields a costlier solve among the three configurations, which is sensible because the solve operation count is cubically proportional to n_Ω assuming fixed basis dimensions (see Table 2).
- (iii) For both DD-LSPG and DD-GNAT, the solve times for both the 2×2 “coarse” and 2×2 “fine” configurations was roughly the same, which is sensible given that these configurations are characterized by the similar basis dimensions and the same number of subdomains (see Table 2).
- (iv) For a fixed error, the port basis type incurred the largest solve wall time compared with the other three basis types; this is sensible because—on average—it has a larger basis dimension compared with the other three types. The skeleton, full-interface and subdomain types yield roughly the same solve cost for a fixed error.

We now analyze assembly wall time⁵ and thus consider the middle column of Figure 7. These figures illustrate the following trends:

- (i) DD-LSPG assembly wall time of four basis types are almost similar, this is due to dominated time/cost of computing the residuals, Jacobians and Hessians as listed on Algorithm 1.
- (ii) For DD-LSPG, the 2×2 “fine” configuration yields the largest assembly wall time because the number of DOFs per subdomain interior n_i^Ω and subdomain boundary n_i^Γ is the largest in this case, and $n_i^{z,r} = n_i^{z,\Omega} = n_i$ and $n_i^{z,\Gamma} = n_i^\Gamma$ for DD-LSPG (see Table 4). On the other hand, the assembly wall time for DD-LSPG is similar in the 2×2 “coarse” and 4×4 “fine” configurations due to these numbers being roughly the same.

⁵Note for all numerical experiments in this paper, the assembly stage is performed in a serial manner (not parallel) for simple implementation. However, the timing on each subdomain is recorded for properly post-assessment.

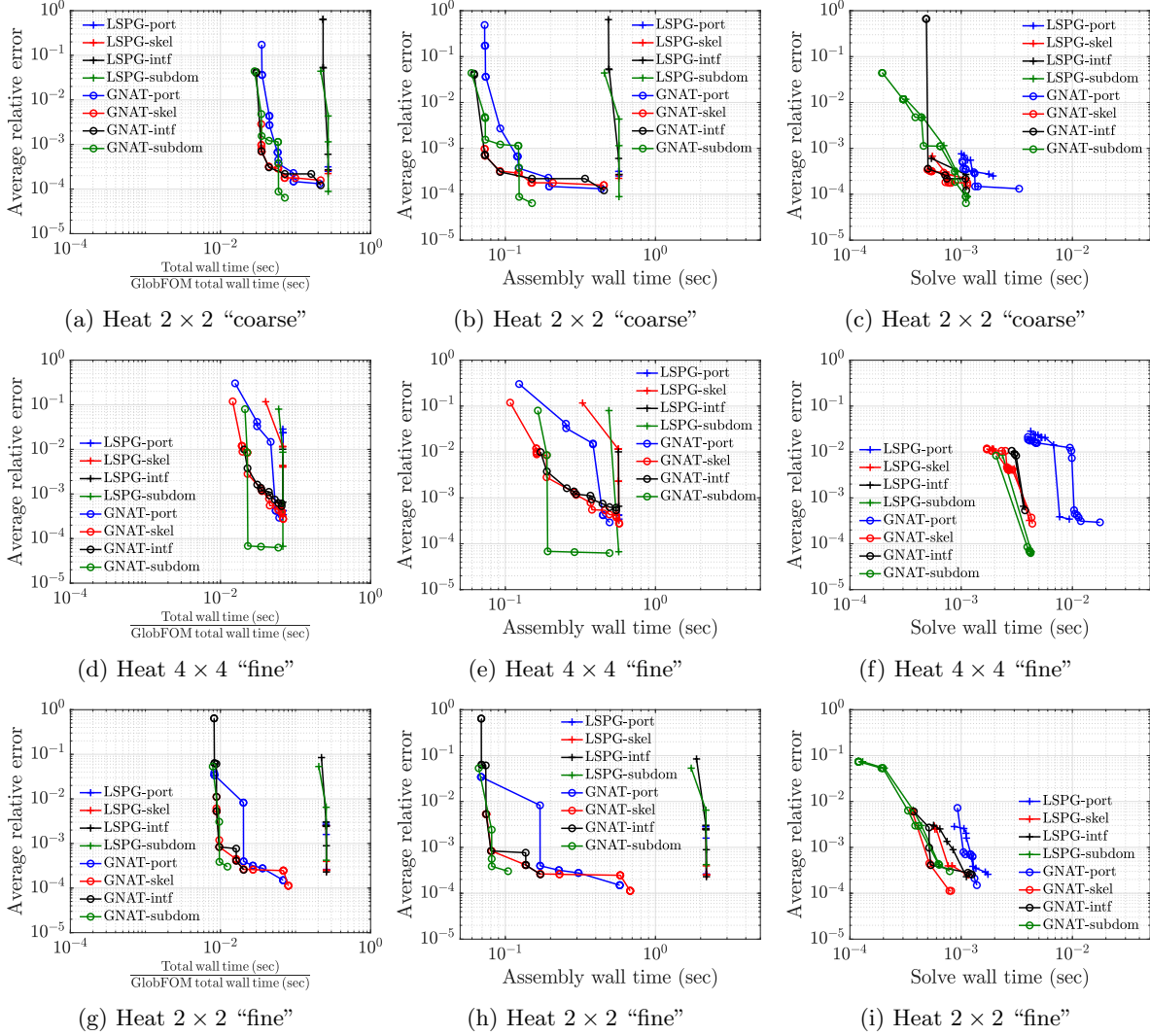
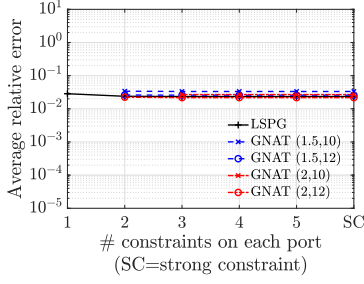
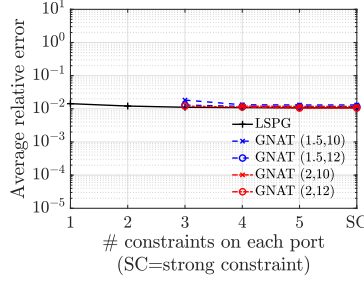


Figure 7: Heat equation, top-down training, Pareto front plots for wall-all (normalized with respect global FEM wall-all timing), wall-assemble and wall-solve timing of three different configurations for varying model parameters reported in Table 8.

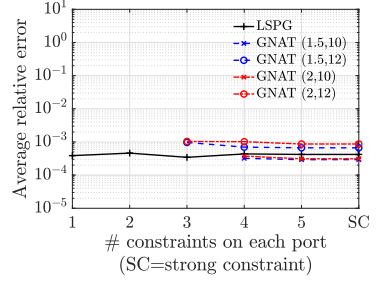
- (iii) Among 3 configurations, the relative performance improvement of DD-GNAT over DD-LSPG (with regard to the assembly wall time) is the smallest in the 4×4 “fine” configuration, while it is the largest for the 2×2 “fine” configuration. This occurs because when each subdomain becomes smaller in size with a modest number of DOFs per subdomain, the subdomain exhibiting the strongest solution nonlinearity requires a relatively large number of sample points (see Figure 6d).
- (iv) Conversely, the relative performance improvement of DD-GNAT over DD-LSPG (with regard to the assembly wall time) is the largest for the 2×2 “fine” configuration because this case corresponds to the largest number of degrees of freedom per subdomain interior and boundary.
- (v) For a fixed accuracy, the port bases (blue curves) almost always yielded a higher assembly wall time than the other basis types; as before, this can be attributed to the larger basis dimensions that typically accompany this basis type.



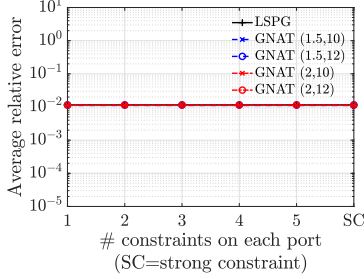
(a) port, $v = 10^{-5}$ on Ω_i , $v = 10^{-5}$ on Γ_i



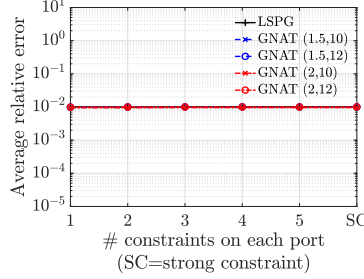
(b) port, $v = 10^{-5}$ on Ω_i , $v = 10^{-8}$ on Γ_i



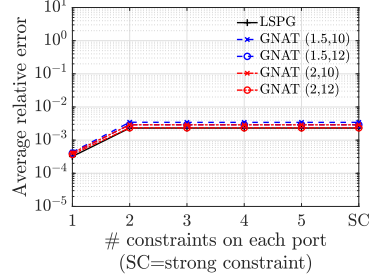
(c) port, $v = 10^{-8}$ on Ω_i , $v = 10^{-8}$ on Γ_i



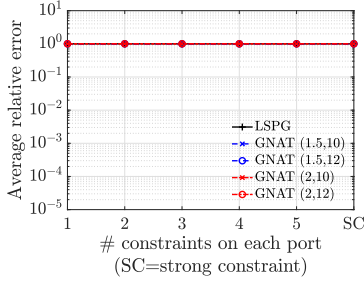
(d) skeleton, $v = 10^{-5}$ on Ω_i , $v = 10^{-5}$ on Γ_i



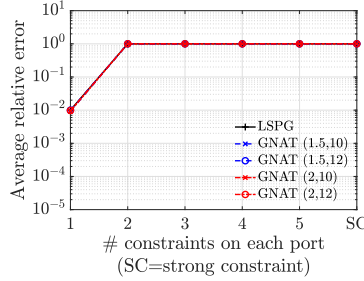
(e) skeleton, $v = 10^{-5}$ on Ω_i , $v = 10^{-8}$ on Γ_i



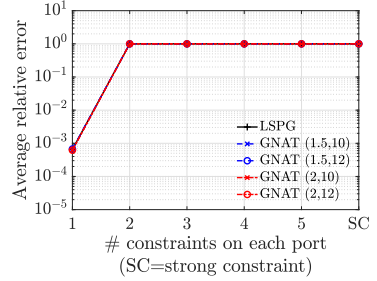
(f) skeleton, $v = 10^{-8}$ on Ω_i , $v = 10^{-8}$ on Γ_i



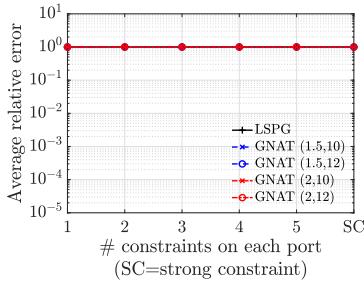
(g) full-interface, $v = 10^{-5}$ on Ω_i , $v = 10^{-5}$ on Γ_i



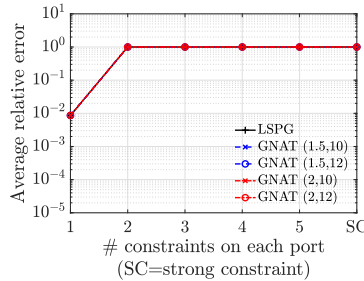
(h) full-interface, $v = 10^{-5}$ on Ω_i , $v = 10^{-8}$ on Γ_i



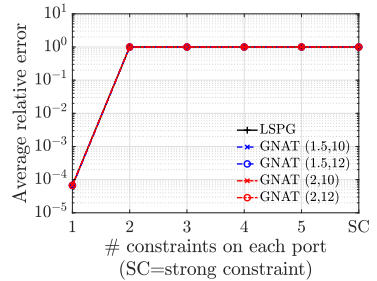
(i) full-interface, $v = 10^{-8}$ on Ω_i , $v = 10^{-8}$ on Γ_i



(j) subdomain, $v = 10^{-5}$



(k) subdomain, $v = 10^{-7}$



(l) subdomain, $v = 10^{-9}$

Figure 8: Heat equation, top-down training, 4×4 “fine” configuration, average relative error (DD-LSPG and DD-GNAT) versus number of constraint per port for varying model parameters reported in Table 8 (SC=strong constraints). In the legend GNAT(x, y) implies the DD-GNAT model with $n_i^z/p_i^r = x$ and $v = 10^{-y}$ for r_i .

Next, we consider the overall wall time, and turn attention to the three subfigures in the leftmost column of Figure 7. From the center and rightmost columns, we see that the assembly wall time dominates the solve wall time in this example; thus, the assembly wall-time behavior is most closely reflected in the overall wall-time performance of the different methods. We see that the DD-GNAT methods can realize $> 100\times$ wall-time speedups relative to the FOM in this case, with DD-LSPG yielding only modest wall-time speedups, which are $< 10\times$ in both the 2×2 “coarse” and “fine” configurations.

Figure 8 shows the average relative error as a function of the number of constraints per port with parameters reported in Table 8 for the 4×4 “fine” configuration. The subfigures in the first two rows of Figure 8 imply that strong compatibility constraints yield better accuracy than weak compatibility for both port and (generally impractical) skeleton basis types. This is sensible, as these basis types ensure that neighboring components have *compatible* bases on shared ports, so weak compatibility constraints lead to no benefit; see Remark 1. On the other hand, the subfigures in the two last rows of Figure 8 show that weak constraint case with only one constraint per port yield the best accuracy for full-interface and full-subdomain basis types. As discussed in Remark 1, this result is expected because neighboring components generally have *incompatible* bases on shared ports for these basis types. The next section will lend additional insight into the behavior of the full-interface and full-subdomain basis types.

8.1.5 Full-interface basis: effect of weak and strong constraints

For illustrative purposes, we investigate further the effects of weak versus strong compatibility constraints for the full-interface basis type (i.e., *incompatible* bases). Due to its similarity, only full-interface bases is discussed here. We consider the parameters for DD-LSPG simulation as follows: 4×4 “fine” configuration, $\boldsymbol{\mu} = (5.005, 5.005)$, full-interface bases, $\nu = 1 - 10^{-5}$ on Ω_i , $\nu = 1 - 10^{-8}$ on Γ_i , and weak constraint cases with one and four constraints per port. Figures 9 visualizes the corresponding solutions of these two cases. These figures verify visually our observations in the previous section and the comments in Remark 1: enforcing weak compatibility with only one constraint per port yields better global solutions despite a larger discrepancy in the solution computed by neighboring subdomains on the interface (Figure 9a–9f), while enforcing additional interface constraints (i.e, four constraints per port in this case) imposes such a strict compatibility condition that the resulting interface solution is simply the trivial solution, yielding significant overall errors despite negligible discrepancies in the solutions computed on neighboring subdomains (Figure 9g–9l).

8.1.6 Subdomain (or bottom-up) training for 4×4 “fine” configuration

Reproductive test

Table 9: Heat equation, bottom-up training, 4×4 “fine” configuration, reproductive test, ROM methods performance at point $\boldsymbol{\mu}_{\text{test}} = (5.005, 5.005) \notin \{\boldsymbol{\mu}_{\text{train}}^j\}_{j=1}^{n_{\text{train}}}$ for one online computation. Recall from Section 6 that $\nu \in [0, 1]$ denotes the energy criterion employed by POD.

train parameter	$\boldsymbol{\mu}_{\text{train}}^i = (5, 5)$ on Ω_i , $1 \leq i \leq n_{\Omega}$					
constraint	strong					
basis	port			full-interface		
method	DD-LSPG	DD-LSPG	DD-LSPG	DD-LSPG	DD-LSPG	DD-LSPG
ν for state	$1 - 10^{-12}$	$1 - 10^{-14}$	$1 - 10^{-17}$	$1 - 10^{-10}$	$1 - 10^{-12}$	$1 - 10^{-17}$
number Newton iter.	9	7	7	8	7	7
rel. error	8.1960×10^{-1}	5.9268×10^{-2}	1.9610×10^{-7}	3.8504×10^{-1}	4.7951×10^{-2}	1.9462×10^{-7}

In this section, we investigate the possibility of subdomain (or bottom-up) training that is opposite to the top-down training in previous sections. The main goal is to create and use snapshots *completely* at component/subdomain level (rather than system/global level like top-down training) to build corresponding reduced bases. In other words, the approach is *completely* bottom-up similar to the SCRBE method [4, 8] except that our proposed approach solves nonlinear PDE, while SCRBE solves linear PDE only. We shall

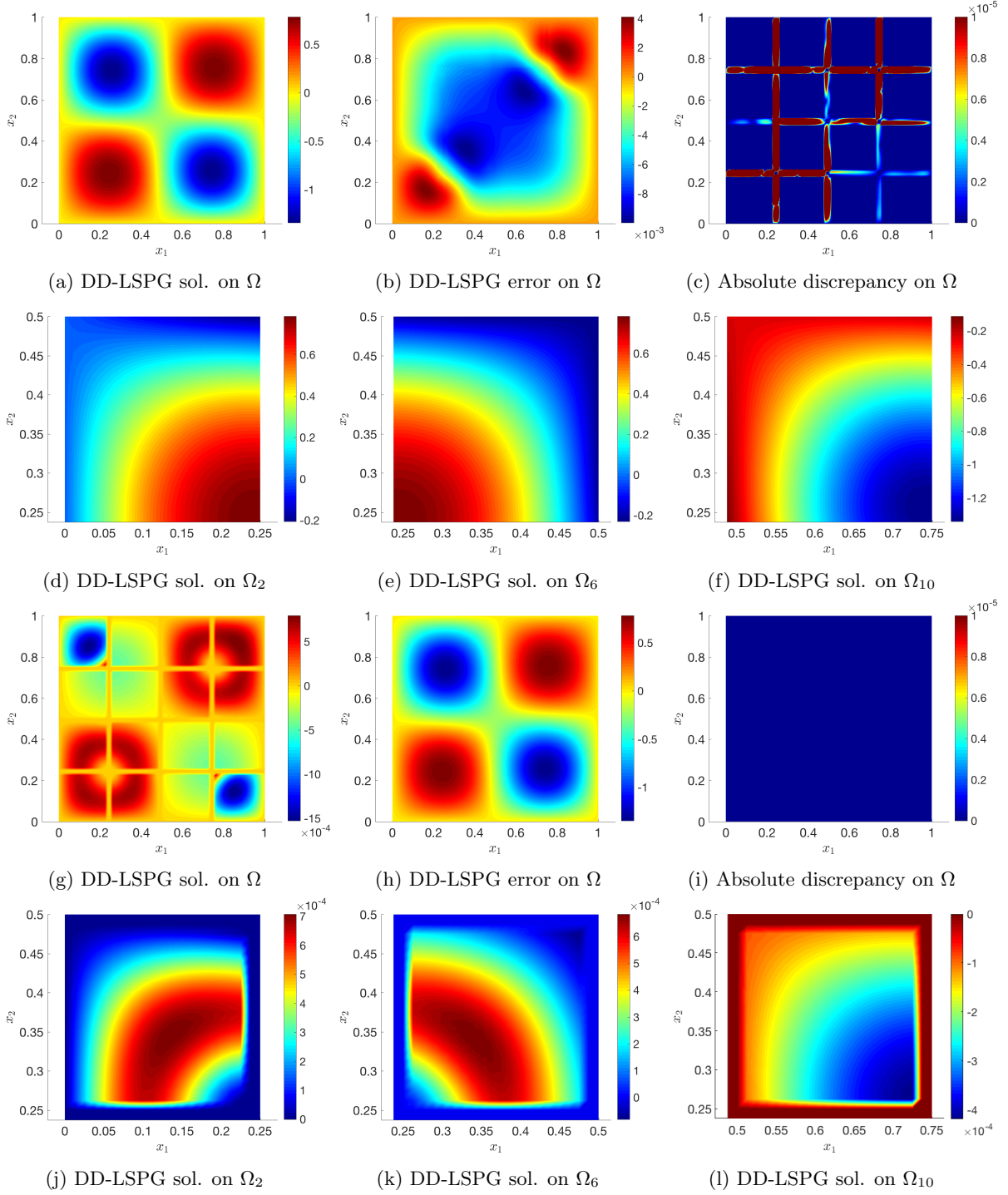


Figure 9: Heat equation, top-down training, 4×4 “fine” configuration, solutions visualization on Ω with full-interface bases and weak constraints: one constraint per port (top 2 rows) versus four constraints per port (last 2 rows).

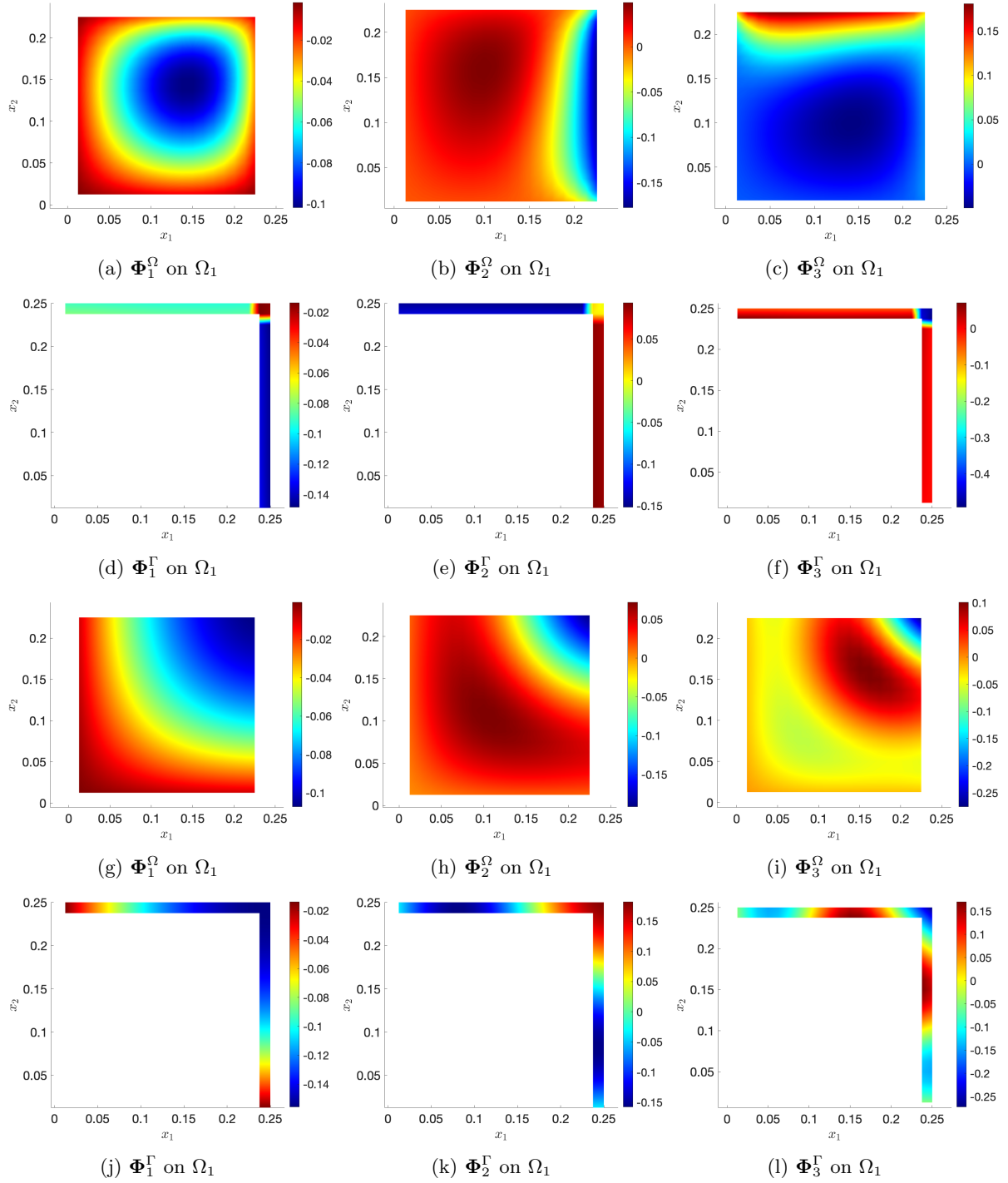


Figure 10: Heat equation, 4×4 “fine” configuration, fixed train parameter, full-interface basis visualization on Ω_1 : bottom-up training (top 2 rows) versus top-down training (last 2 rows).

describe a specific approach that borrows ideas of SCRBE (algorithm 2, page 279 of [48]) to build such bottom-up reduced bases.

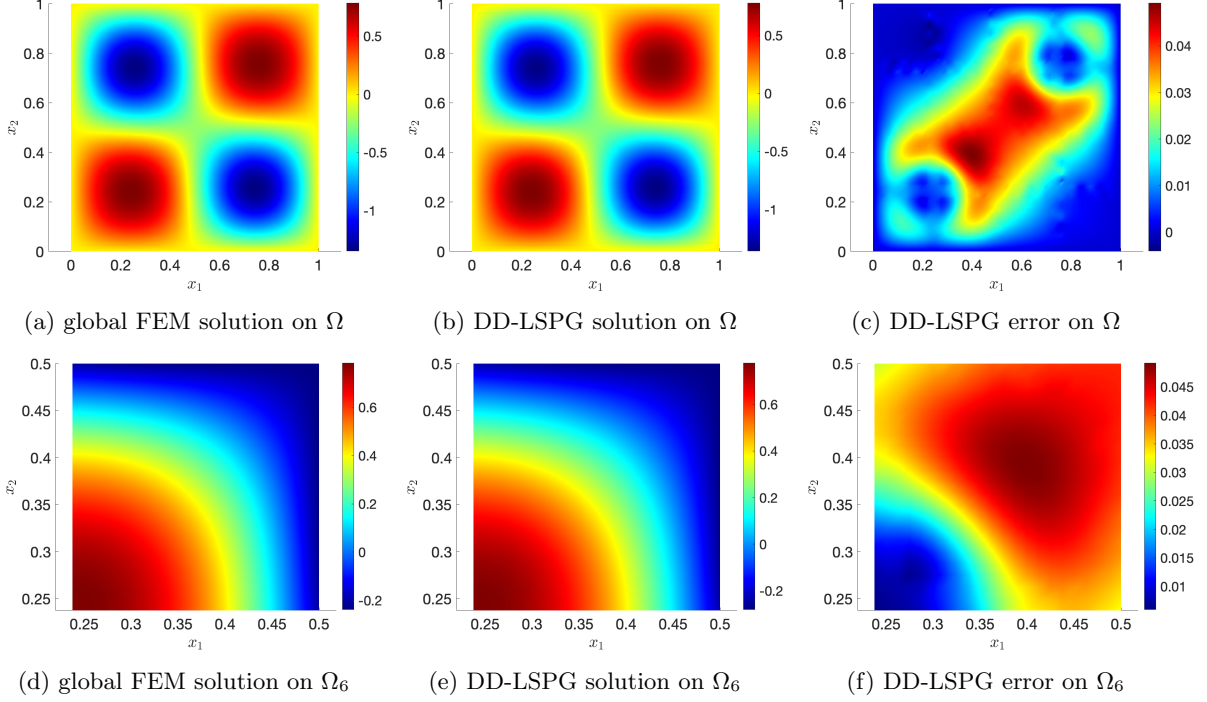


Figure 11: Heat equation, bottom-up training, 4×4 “fine” configuration, reproductive test, full-interface bases ($\nu = 1 - 10^{-12}$) in Table 9, solutions visualized on Ω and Ω_6 .

Table 10: Heat equation, bottom-up training, 4×4 “fine” configuration, reproductive test, ROM parameters on first four Ω_i ($1 \leq i \leq 4$) resulting from Table 9.

basis	port				full-interface			
	$1 - 10^{-14}$				$1 - 10^{-12}$			
subdomains	Ω_1	Ω_2	Ω_3	Ω_4	Ω_1	Ω_2	Ω_3	Ω_4
n_A	984				984			
$p_i^\Omega (n_i^\Omega)$	25 (324)	38 (324)	36 (324)	25 (342)	17 (324)	26 (324)	25 (324)	17 (342)
$p_i^\Gamma (n_i^\Gamma)$	76 (76)	116 (116)	116 (116)	78 (78)	72 (76)	110 (116)	110 (116)	74 (78)
$p_1^p (n_1^p)$	36 (36)	36 (36)	36 (36)	36 (36)				
$p_2^p (n_2^p)$	4 (4)	4 (4)	4 (4)	4 (4)				
$p_3^p (n_3^p)$	36 (36)	36 (36)	36 (36)	38 (38)				
$p_4^p (n_4^p)$		4 (4)	4 (4)					
$p_5^p (n_5^p)$		36 (36)	36 (36)					

We choose the 4×4 “fine” configuration and loop over all ports on all subdomains. On each port, we do the following:

1. Build a set of 1D Legendre polynomials that correspond with each edge of the port. For our particular FOM model, a port is a rectangle with x -line and y -line, thus we build 1D Legendre polynomials associated with these 2 lines.
2. Perform tensor product of these 1D Legendre polynomials to create 2D Legendre polynomials of that port. We denote these 2D Legendre polynomials $L_{m,j}^k$ where k is the sequence index, m denotes

subdomain index, and j is port index. (Note that we use same notation as algorithm 2, page 279 of [48].)

3. Perform random linear combinations of these 2D Legendre polynomials to create associated boundary conditions on that port:

$$\mathbf{x}|_{P_j} = \sum_{k=1}^{n_{i,j}^p} r \frac{1}{k^\eta} L_{i,j}^k, \quad 1 \leq i \leq n_\Omega, \quad (8.3)$$

where r is a random variable with univariate uniform density over $(-1,1)$, η is a tuning parameter related to anticipated regularity. For our problem, we also choose $\eta = 2$ following [48].

4. Assemble all the above ‘‘port boundary conditions’’ to form associated boundary conditions on the interface of that subdomain:

$$\mathbf{x}|_{\Gamma_i} = \bigcup_{j \in Q(i)} \mathbf{x}|_{P_j}, \quad 1 \leq i \leq n_\Omega. \quad (8.4)$$

5. Solve the FOM problem of that subdomain Ω_i with ‘‘interface boundary conditions’’ specified above to obtain a *subdomain* FOM solution (or snapshot). Repeat this step with many random linear combinations to create many different interface boundary conditions to collect *subdomain* snapshots, and store them to a *subdomain* snapshots set. For our problem, we perform 200 random ‘‘interface boundary conditions’’ on each subdomain Ω_i , solve the subdomain FOM problems to collect 200 snapshots over each Ω_i , $1 \leq i \leq n_\Omega$, respectively. Note also that we fix the input parameter $\boldsymbol{\mu}_{\text{train}} = (5, 5)$ for all FOM solves over all subdomains Ω_i , $1 \leq i \leq n_\Omega$.
6. With available *subdomain* snapshots set, implement sections 6.1 and/or 6.2 to form corresponding reduced bases.

With bottom-up reduced bases created above, we now compare the DD-LSPG method for fixed values of their parameters, and for the selected online point $\boldsymbol{\mu}_{\text{test}} = (5.005, 5.005)$. Table 9 reports the chosen input parameters and associated performance of the DD-LSPG method, while the resulting ROM parameters over first four subdomains Ω_i , $1 \leq i \leq 4$ are listed on Table 10. Table 9 shows that the produced ROM solutions are converged and get more accurate with increasing number of bases.

Figure 10 compares first three full-interface bases on Ω_1 using bottom-up training (top 2 rows) and top-down training (last 2 rows). As observed from this figure, we see that the quality of bottom-up training bases are not as good as that of top-down training. (This is sensible because the subdomain *completely* not know anything about the global solution.) As a result, bottom-up training uses much more interior and interfaces bases than top-down training does with same accuracy level (comparing Table 6 with Table 9, and Table 7 with Table 10; especially on Table 10, bottom-up training uses *all* available interface bases). This leads to two important consequences: i) we obtain very little dimension reduction on the interface (although still big dimension reduction on the interior) for bottom-up training; ii) bottom-up training must use strong constraint to obtain good converged solutions. This is completely opposite to top-down training where number of interior and interface bases are small (compared with bottom-up training), hence weak constraints are necessary to obtain converged solutions (see Figure 8i). Figure 11 visualizes DD-LSPG solutions and error for the full-interface bases case: it shows that DD-LSPG yield accurate results for full-interface bases with strong constraints using bottom-up training approach.

Predictive test

Finally, we perform a truly predictive test for our proposed framework using bottom-up training. We vary the training parameters on each subdomain so that they are all different from each other, and they also differ from the online testing parameter. In particular, we repeat the workflow 1–6 above to build the bottom-up bases except at step 5 we set $\boldsymbol{\mu}_{\text{train}}^i$ equidistant over subdomains Ω_i , i.e., $\boldsymbol{\mu}_{\text{train}}^i = (\mu_t^i, \mu_i^i)$ on Ω_i , where $\mu_i^i = \frac{\mu_{\text{max}} - \mu_{\text{min}}}{n_\Omega - 1} (i - 1) + \mu_{\text{min}}$, $1 \leq i \leq n_\Omega$. (Namely, $\boldsymbol{\mu}_{\text{train}}^1 \neq \boldsymbol{\mu}_{\text{train}}^2 \neq \dots \neq \boldsymbol{\mu}_{\text{train}}^{n_\Omega} \neq \boldsymbol{\mu}_{\text{test}}$.)

We again compare the DD-LSPG method for fixed values of their parameters, and for the selected online point $\boldsymbol{\mu}_{\text{test}} = (5.005, 5.005)$. Table 11 reports the chosen input parameters and associated performance of

Table 11: Heat equation, bottom-up training, 4×4 “fine” configuration, predictive test, ROM methods performance at point $\boldsymbol{\mu}_{\text{test}} = (5.005, 5.005) \notin \{\boldsymbol{\mu}_{\text{train}}^j\}_{j=1}^{n_{\text{train}}}$ for one online computation. Recall from Section 6 that $v \in [0, 1]$ denotes the energy criterion employed by POD.

train parameter	$\boldsymbol{\mu}_{\text{train}}^i = (\mu_t^i, \mu_i^i)$ on Ω_i , where $\mu_t^i = \frac{\mu_{\text{max}} - \mu_{\text{min}}}{n_{\Omega} - 1}(i - 1) + \mu_{\text{min}}, 1 \leq i \leq n_{\Omega}$			
constraint	strong			
basis	port		full-interface	
method	DD-LSPG	DD-LSPG	DD-LSPG	DD-LSPG
v for state	$1 - 10^{-15}$	$1 - 10^{-17}$	$1 - 10^{-15}$	$1 - 10^{-17}$
number Newton iter.	7	7	7	7
rel. error	9.9537×10^{-2}	2.6104×10^{-3}	9.9537×10^{-2}	2.6104×10^{-3}

Table 12: Heat equation, bottom-up training, 4×4 “fine” configuration, predictive test, ROM parameters on first four Ω_i ($1 \leq i \leq 4$) resulting from Table 11.

basis	port				full-interface			
v for state	$1 - 10^{-17}$				$1 - 10^{-17}$			
subdomains	Ω_1	Ω_2	Ω_3	Ω_4	Ω_1	Ω_2	Ω_3	Ω_4
n_A	984				984			
$p_i^{\Omega} (n_i^{\Omega})$	200 (324)	200 (324)	200 (324)	200 (342)	200 (324)	200 (324)	200 (324)	200 (342)
$p_i^{\Gamma} (n_i^{\Gamma})$	76 (76)	116 (116)	116 (116)	78 (78)	72 (76)	110 (116)	110 (116)	74 (78)
$p_1^p (n_1^p)$	36 (36)	36 (36)	36 (36)	36 (36)				
$p_2^p (n_2^p)$	4 (4)	4 (4)	4 (4)	4 (4)				
$p_3^p (n_3^p)$	36 (36)	36 (36)	36 (36)	38 (38)				
$p_4^p (n_4^p)$		4 (4)	4 (4)					
$p_5^p (n_5^p)$		36 (36)	36 (36)					

the DD-LSPG method, while the resulting ROM parameters over first four subdomains $\Omega_i, 1 \leq i \leq 4$ are listed on Table 12. Table 11 shows that the produced ROM solutions are converged and accurate. However, comparing Table 9 with 11, and Table 10 with 12 show that predictive testing takes many more interior bases than reproductive testing with same accuracy level (and both testing cases use same number of interface bases). This is also sensible because the predictive testing case is usually more general and more challenging than the reproductive testing case.

8.2 Parameterized Burgers’ equation

8.2.1 Exact solution and global FD discretization

Table 13: Burgers equation, parameters for the exact solution

Parameter	ν	x_1^0	a_2	a_3	a_4	a_5	a_1	λ
Value	0.1	1	a_1	0	0	1	$\in [1, 10000]$	$\in [5, 25]$

We now consider a parameterized 2D steady state Burgers’ equation described in Ref. [49]. The problem consists of computing the velocity field $\mathbf{u} \equiv (u_1, u_2)$ that satisfies

$$\mathbf{u} \cdot \nabla \mathbf{u} = \nu \nabla^2 \mathbf{u}, \quad (8.5)$$

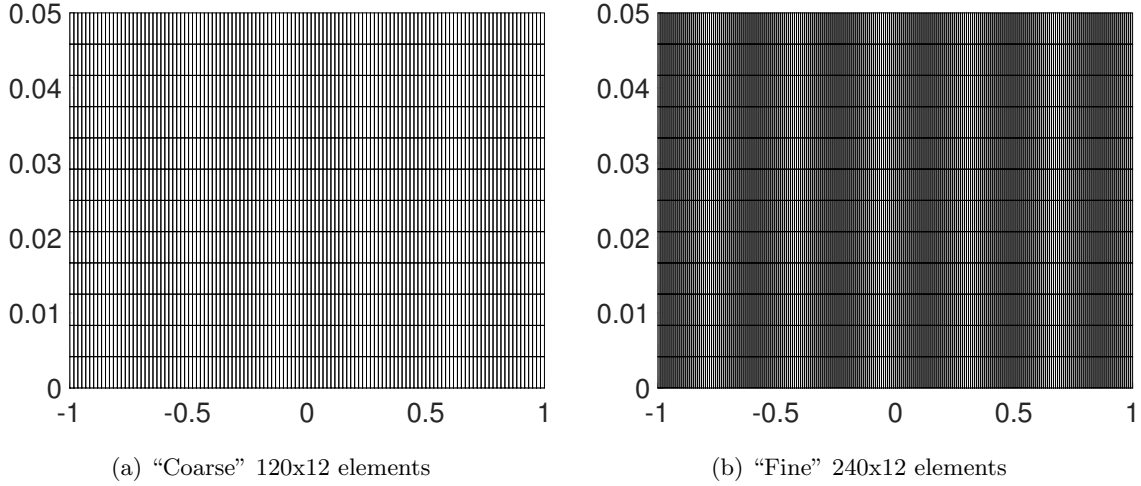


Figure 12: Burgers' equation. Two global FD mesh used for discretization.

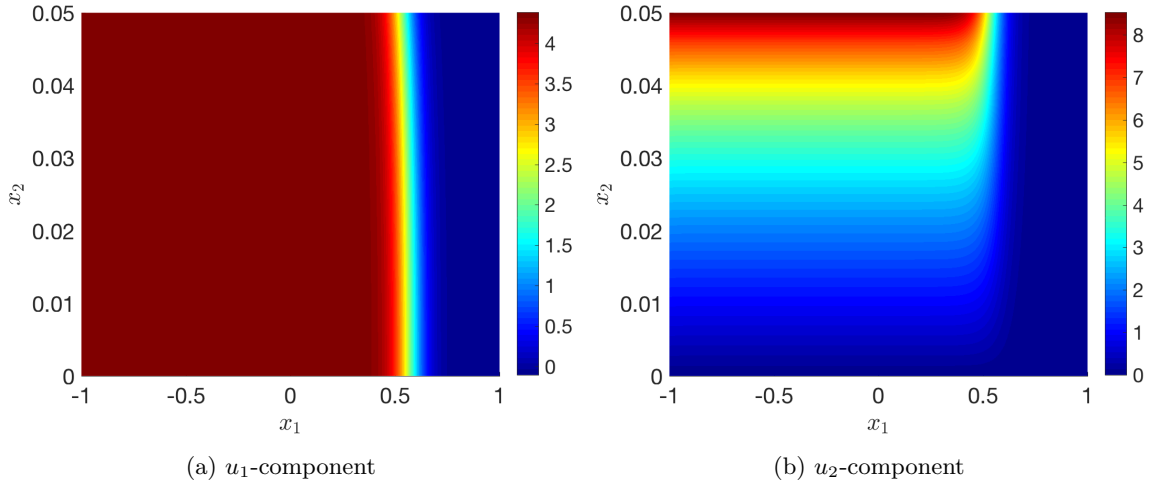


Figure 13: Burgers' equation, global FD solution for $\mu = (7692.5384, 21.9230)$ using "fine" FD mesh 240x12 elements.

Table 14: Burgers equation, parameters for global FD discretization

	"Coarse" mesh	"Fine" mesh
Number of elements	1440	2880
Number of nodes	1573	3133
n	2618	5258

where ν is the viscosity coefficient, $\mathbf{x} = (x_1, x_2) \in \Omega = [-1, 1] \times [0, 0.05]$. Nonhomogenous Dirichlet boundary conditions (on $\Gamma \equiv \partial\Omega$) for the numerical solutions are taken directly from the exact solution that is defined

as follows

$$\begin{aligned} u_1 &= -2\nu \left[a_2 + a_4 x_2 + \lambda a_5 \left(e^{\lambda(x_1 - x_1^0)} + e^{-\lambda(x_1 - x_1^0)} \right) \cos(\lambda x_2) \right] / \Phi, \\ u_2 &= -2\nu \left[a_3 + a_4 x_2 - \lambda a_5 \left(e^{\lambda(x_1 - x_1^0)} + e^{-\lambda(x_1 - x_1^0)} \right) \sin(\lambda x_2) \right] / \Phi, \end{aligned} \quad (8.6)$$

where $\Phi = a_1 + a_2 x_1 + a_3 x_2 + a_4 x_1 x_2 + a_5 \left(e^{\lambda(x_1 - x_1^0)} + e^{-\lambda(x_1 - x_1^0)} \right) \cos(\lambda x_2)$, and $a_i, i = 1, \dots, 5, \lambda$ and x_1^0 are given scalars. To parameterize the problem, these parameters are given on Table 13, and the input parameter $\boldsymbol{\mu}$ is defined as $\boldsymbol{\mu} \equiv (\mu_1, \mu_2) = (a_1, \lambda) \in \mathcal{D} = [1, 10000] \times [5, 25]$.

We use the finite-difference method with three-point centered difference scheme and uniform grid to discretize Eq. (8.5). The exact solution on the boundary Γ is used as nonhomogeneous Dirichlet boundary condition to solve for the interior unknown nodes. Analogously to the previous example, we also employ a ‘‘coarse’’ and ‘‘fine’’ mesh, characterized by 1440 (120×12) and 2880 (240×12) quadrilateral elements, respectively. Figure 12 depicts these meshes, while Table 14 reports the corresponding parameters. We emphasize that this problem is characterized by two degrees of freedom per node as opposed to the previous example. Figure 13 plots the FD reference solution on the ‘‘fine’’ mesh with $\boldsymbol{\mu} = (7692.5384, 21.9230)$. As observed from Figure 13, the solution presents a shock which is characterized by $\boldsymbol{\mu} = (a_1, \lambda)$, where a_1 relates to the distance of the shock from the left edge and λ relates to the steepness of the shock, respectively.

8.2.2 Full-order model

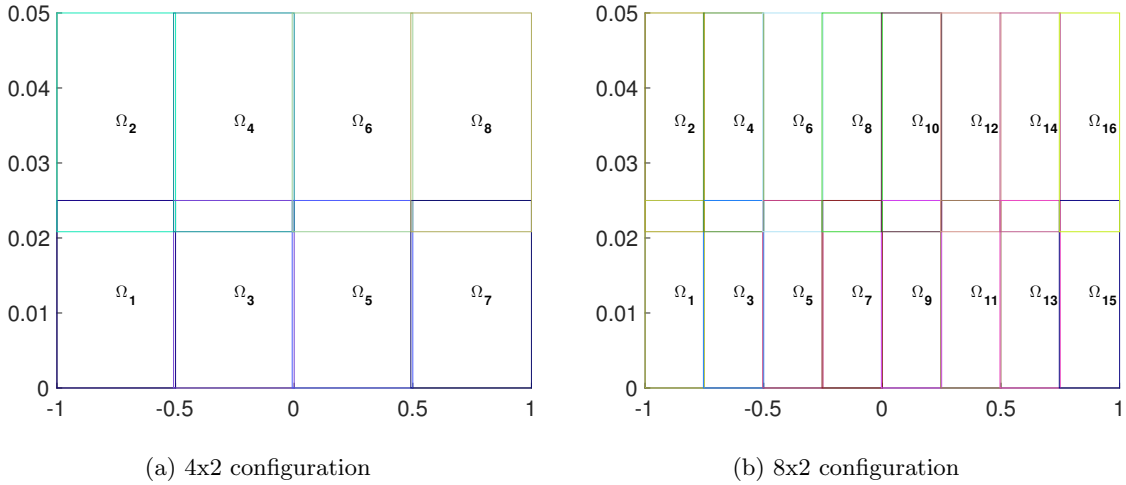


Figure 14: Burgers’ equation, two domain-decomposition configurations based on the finite-difference mesh.

Table 15: Burgers equation, parameters used for three FOM configurations

	4x2 ‘‘coarse’’	8x2 ‘‘fine’’	4x2 ‘‘fine’’
n_Ω	8	16	8
$n_{\bar{A}}$	704	1488	1184
n_p	13	29	13
# DOFs on Ω_1	434	434	854
# nodes on Ω_1	217	217	427
	weak scaling		
		strong scaling	

Table 16: Burgers equation, parameters on each Ω_i for the 4×2 “fine” configuration. In this case, there are $n_p = 13$ total ports with $n_1^p = 16$, $n_2^p = 232$, $n_3^p = 20$, $n_4^p = 16$, $n_5^p = 232$, $n_6^p = 20$, $n_7^p = 16$, $n_8^p = 232$, $n_9^p = 20$, $n_{10}^p = 236$, $n_{11}^p = 8$, $n_{12}^p = 8$, $n_{13}^p = 8$.

	Ω_1	Ω_2	Ω_3	Ω_4	Ω_5	Ω_6	Ω_7	Ω_8
n_i^r	590	708	600	720	600	720	600	720
n_i^Ω	464	580	464	580	464	580	472	590
n_i^Γ	256	260	280	288	280	288	260	264
$n_i (= n_i^\Omega + n_i^\Gamma)$	720	840	744	868	744	868	732	854
Number of subdomain ports $ Q(i) $	3	3	5	5	5	5	3	3

After applying the finite-difference discretization, we introduce the algebraically non-overlapping decomposition of the problem described in Section 2. As in the previous example, the chosen algebraic decomposition corresponds to a spatial domain decomposition in space. In particular, we employ decompositions into both 4×2 (such that $n_\Omega = 8$) and 8×2 (such that $n_\Omega = 16$) configurations as depicted in Figure 14. Table 15 lists the parameters used for each of these configurations. The pairwise comparison of the 4×2 “coarse” and 8×2 “fine” configurations is interpreted as weak scaling, while the pairwise comparison of the 4×2 “fine” and 8×2 “fine” configurations interpreted as strong scaling, respectively. For reference, Table 16 reports the parameters characterizing each subdomain Ω_i , $i = 1, \dots, n_\Omega$ of the 4×2 “fine” configuration.

8.2.3 DD-LSPG and DD-GNAT approximations: one online computation

Table 17: Burgers 4×2 “fine” configuration, ROM methods performance at point $\boldsymbol{\mu} = (7692.5384, 21.9230) \notin \{\boldsymbol{\mu}_{\text{train}}^j\}_{j=1}^{n_{\text{train}}}$ for one online computation. Recall from Section 6 that $v \in [0, 1]$ denotes the energy criterion employed by POD.

constraint	strong							
	port		skeleton		full-interface		subdomain	
method	DD-LSPG	DD-GNAT	DD-LSPG	DD-GNAT	DD-LSPG	DD-GNAT	DD-LSPG	DD-GNAT
v for state	$1 - 10^{-4}$	$1 - 10^{-4}$	$1 - 10^{-4}$	$1 - 10^{-4}$	$1 - 10^{-4}$	$1 - 10^{-4}$	$1 - 10^{-5}$	$1 - 10^{-5}$
v for residual		$1 - 10^{-8}$		$1 - 10^{-8}$		$1 - 10^{-8}$		$1 - 10^{-8}$
n_i^z / p_i^r		2		2		2		2
rel. error	0.0073	0.0077	0.0109	0.0108	0.7982	0.7917	1.0000	1.0000
speedup	15.62	23.06	13.93	20.30	12.51	18.48	31.17	46.80

We apply the same procedure described in Section 8.1.3 to generate the reduced bases required for the reduced-order models. In particular, we solve the FOM (2.1) for $\boldsymbol{\mu} \in \{\boldsymbol{\mu}_{\text{train}}^j\}_{j=1}^{n_{\text{train}}} \subset \mathcal{D}$, where we again define the training-parameter set $\{\boldsymbol{\mu}_{\text{train}}^j\}_{j=1}^{n_{\text{train}}}$ according to a 20×20 equispaced sampling of the parameter domain \mathcal{D} , yielding $n_{\text{train}} = 400$ samples. We then apply the methods described in Section 6 to create port, skeleton, full-interface, and full-subdomain bases from these training data. At each iteration of the Newton–Raphson algorithm used to solve the FOM equations (2.1), the residual vector is saved, and the resulting residual snapshots are employed to generate the residual bases $\boldsymbol{\Phi}_i^r$, $i = 1, \dots, n_\Omega$ that are used by DD-GNAT via POD. Lastly, the GNAT offline algorithm 4 is performed to create sample meshes \mathfrak{s}_i for all subdomains Ω_i .

We now compare the methods DD-LSPG and GNAT for fixed values of their parameters, and for the randomly selected online point $\boldsymbol{\mu} = (7692.5384, 21.9230) \notin \{\boldsymbol{\mu}_{\text{train}}^j\}_{j=1}^{n_{\text{train}}}$. Table 17 reports the chosen input parameters and associated performance of the methods, while the resulting ROM parameters over first four subdomains Ω_i are listed on Table 18. Again, the results on Table 17 confirm the comments in Remark 1, which suggested that enforcing strong compatibility can yield poor results for full-interface

Table 18: Burgers 4×2 “fine” configuration, ROM parameters on first four $\Omega_i (1 \leq i \leq 4)$, resulting from Table 17.

basis	port				skeleton				full-interface				subdomain			
	Ω_1	Ω_2	Ω_3	Ω_4	Ω_1	Ω_2	Ω_3	Ω_4	Ω_1	Ω_2	Ω_3	Ω_4	Ω_1	Ω_2	Ω_3	Ω_4
n_A	69				84				48				78			
p_i^Ω	3	4	4	5	3	4	4	5	3	4	4	5	5	6	8	9
p_i^Γ	9	10	17	19	12	12	12	12	3	4	5	6	5	6	8	9
p_1^p	3	3	3	4												
p_2^p	3	3	3	3												
p_3^p	3	4	5	5												
p_4^p			3	3												
p_5^p			3	4												
n_i^z	80	88	108	124	80	88	108	124	80	88	108	124	80	88	108	124
p_i^r	40	44	54	62	40	44	54	62	40	44	54	62	40	44	54	62

and full-subdomain bases, and that only port and skeleton bases are well-suited for strong compatibility constraints. Figure 15 visualizes the DD-LSPG and DD-GNAT solutions for the port-bases case; it shows that DD-LSPG and DD-GNAT yield accurate results for port bases with strong constraints as anticipated.

8.2.4 DD-LSPG and DD-GNAT approximations: parameter study

Table 19: Burgers equation, ROM-method parameters limits for parameter study (skel.=skeleton, intf.=full-interface, subdom.=subdomain). Recall from Section 6 that $v \in [0, 1]$ denotes the energy criterion employed by POD.

method	DD-LSPG	GNAT
v on Ω_i for interior/boundary bases	$\{1 - 10^{-4}, 1 - 10^{-7}\}$	$\{1 - 10^{-4}, 1 - 10^{-7}\}$
v on Γ_i for interior/boundary bases	$\{1 - 10^{-4}, 1 - 10^{-7}\}$	$\{1 - 10^{-4}, 1 - 10^{-7}\}$
v for full-subdomain bases	$\{1 - 10^{-5}, 1 - 10^{-6}, 1 - 10^{-7}, 1 - 10^{-9}\}$	$\{1 - 10^{-5}, 1 - 10^{-6}, 1 - 10^{-7}, 1 - 10^{-9}\}$
v for r_i		$\{1 - 10^{-4}, 1 - 10^{-6}, 1 - 10^{-8}, 1 - 10^{-10}\}$
n_i^z/p_i^r		$\{1, 1.5, 2, 4\}$
number of constraints	$\{1, 2, 3, 4, 5, \text{strong}\}$	$\{1, 2, 3, 4, 5, \text{strong}\}$
basis types	$\{\text{port, skel., intf., subdom.}\}$	$\{\text{port, skel., intf., subdom.}\}$

We again compare the performance of the ROM methods across a wide variation of all method parameters. Table 19 reports the tested parameter values for each method. We employ the same approach to reporting wall times as previously described in Section 8.1.4. Again, as described previously in Section 8.1.4, we then construct a Pareto front for each method. Figure 16 reports these Pareto fronts, while Figure 17 plots the average relative error versus number of constraints per port for the 4×2 “fine” configuration.

Comparing Figures 16 and 7 illustrates that nearly identical overall trends are apparent for the two examples; we thus refer to the discussion in Section 8.1.4 to provide the primary interpretations for the current case. The primary difference between the previous example and the current one is that the full-subdomain bases outperform the full-interface bases in this case and thus yield the best overall performance;

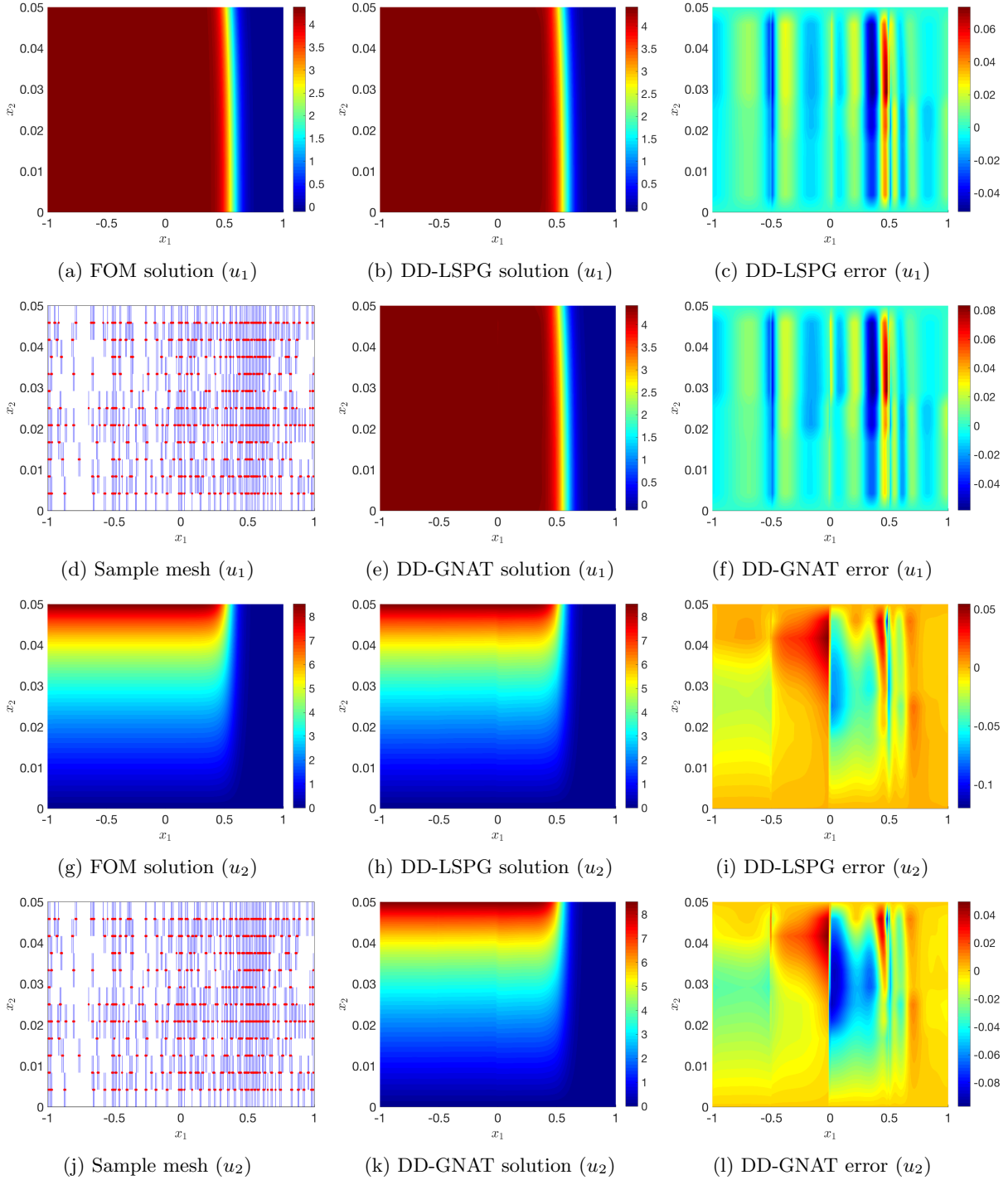


Figure 15: Burgers equation, 4x2 “fine” configuration, port bases in Table 17, solutions visualized on Ω .

further, the skeleton basis yields worse wall-time performance for smaller errors compared with the port bases in the present example. We emphasize that—as in the previous example—DD-GNAT yields the best overall performance, achieving $> 50\times$ speedup with $< 1\%$ relative error, and performs best with the full-subdomain

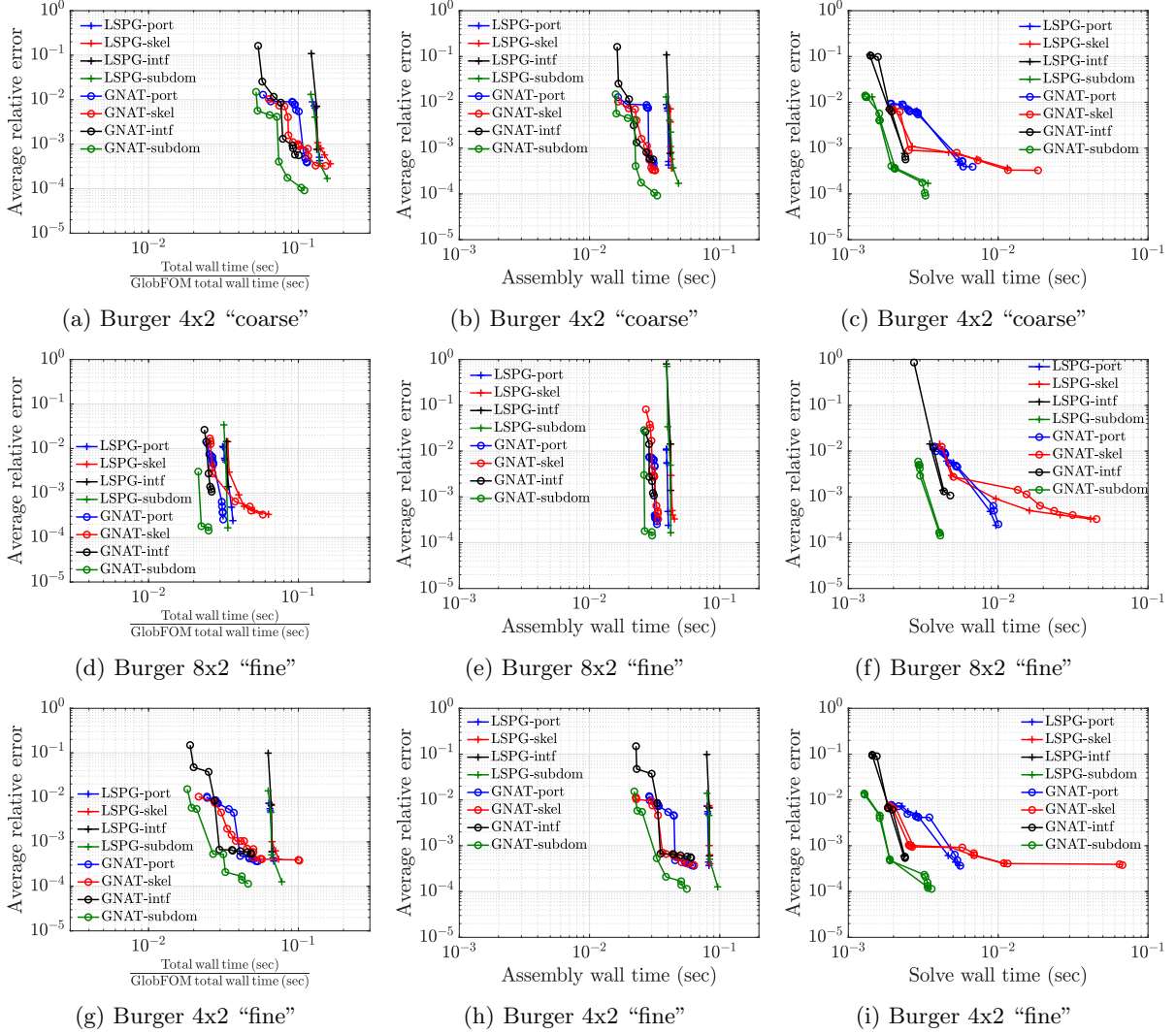


Figure 16: Burgers’ equation, Pareto front plots for wall-all (normalized with respect global FOM wall-all timing), wall-assemble and wall-solve timing of three different configurations for parameters reported in Table 19.

basis in this case.

Lastly, Figure 17 reports the average relative error as a function of the number of constraints per port with parameters reported in Table 19 for the 4x2 “fine” configuration. Again, comparing Figures 17 and 8 illuminate that nearly identical overall trends are observed in this example as in the previous one. In particular, the subfigures in the top two rows of Figure 17 imply that strong compatibility constraints yield better accuracy than weak compatibility for both port and skeleton basis types, while the two last rows show that weak constraint case with a small number of constraints per port yield the best accuracy for full-interface and full-subdomain basis types. The discussion in Remark 1 accounts for this behavior: approaches that ensure neighboring components have *compatible* bases on shared ports perform best with strong compatibility constraints, while approaches that allow for neighboring components to have *incompatible* bases on shared ports perform best with weak compatibility constraints.

9 Conclusions

This work proposed the domain-decomposition least-squares Petrov–Galerkin (DD-LSPG) model-reduction method applicable to parameterized systems of nonlinear algebraic equations. In contrast to previous works, we adopt an algebraically non-overlapping decomposition strategy, allowing it to be applicable to multiple discretization techniques in the case of parameterized PDEs; further, in contrast with previous DDROM methods for nonlinear systems, it is a “complete ROM” approach rather than a hybrid ROM/FOM technique. We equipped DD-LSPG with hyper-reduction, four different strategies for constructing subdomain bases, supported both strong and weak compatibility constraints, and proposed an SQP solver that exposes parallelization. Further, we developed both *a posteriori* and *a priori* error bounds for the technique. Numerical experiments revealed several interesting performance attributes of the DD-LSPG methodology:

1. The best type of compatibility constraint is strongly dependent on the type of subdomain bases; in particular, subdomain bases that admit basis incompatibilities on shared interfaces (i.e., full-interface and full-subdomain bases) require weak compatibility constraints to avoid trivial interface solutions, while subdomain bases that guarantee shared-interface compatibility (i.e., port and skeleton bases) perform well with strong constraints.
2. Hyper-reduction is essential to keep assembly costs low when the number of DOFs per subdomain is large; this is evidenced by the substantial performance gains of DD-GNAT over DD-LSPG for such cases.
3. The best overall performance was achieved by full-subdomain and full-interface bases that employed weak compatibility constraints, with the worst performance obtained by port bases, as the latter case generally yields a large number of interface DOFs compared with the other approaches. Skeleton bases generally yielded intermediate performance, but are impractical for truly extreme-scale problems or decomposable systems, as they require full-system snapshots to be constructed.
4. Bottom-up training is possible and promising with our proposed framework although more research needs to be done to make it more mature.

Our proposed DD-ROM method is less efficient than the monolithic ROM approach in the online phase because the monolithic ROM approach can produce a smaller number of reduced bases than our method. However, our method introduces a way of accomplishing a domain-decomposition ROM that can be useful for truly large-scale problems where the monolithic ROM may not be feasible due to expensive training phase, e.g., insufficient memory (thanks to bottom-up training). Indeed, while reduced-order models have demonstrated success in many applications across computational science and engineering, they encounter challenges when applied both to nonlinear extreme-scale models due to the prohibitive cost of generating requisite training data, and to decomposable systems due to many-query problems (e.g., design [50, 51, 52, 53]) often requiring repeated reconfigurations of system components. We believe that our current work is a step toward addressing these challenges.

Future work will consider application to truly large-scale problems, alternative parallel numerical solvers for DD-LSPG, more efficient “bottom-up” training strategies that does not require full-system snapshots and thus make the approach directly amenable to extreme-scale and decomposable systems, considering time-dependent problems, and supporting nonlinear trial manifolds [54, 55] for subdomains rather than strictly linear subspaces spanned by reduced bases [56, 57, 58]. We will also consider spatially distributed parameter-dependent problems because the DD-ROM should be able to handle such a high dimensional parameter space efficiently.

Acknowledgements

This paper describes objective technical results and analysis. Any subjective views or opinions that might be expressed in the paper do not necessarily represent the views of the U.S. Department of Energy or the United

States Government. Sandia National Laboratories is a multimission laboratory managed and operated by National Technology and Engineering Solutions of Sandia, LLC., a wholly owned subsidiary of Honeywell International, Inc., for the U.S. Department of Energy's National Nuclear Security Administration under contract DE-NA-0003525.

A Offline computational procedure for GNAT

A.1 Formation of residual bases

Given a residual-snapshot matrix $\mathbf{X}_g^r = [\mathbf{r}^1(\mathbf{x}; \boldsymbol{\mu}_{\text{train}}^1), \dots, \mathbf{r}^{k_1}(\mathbf{x}; \boldsymbol{\mu}_{\text{train}}^1), \dots, \mathbf{r}^1(\mathbf{x}; \boldsymbol{\mu}_{\text{train}}^{n_{\text{train}}}), \dots, \mathbf{r}^{k_{n_{\text{train}}}}(\mathbf{x}; \boldsymbol{\mu}_{\text{train}}^{n_{\text{train}}})] \in \mathbb{R}^{n \times \sum_{j=1}^{n_{\text{train}}} k_j}$, where k_j is the number of Newton iterations associated with parameter $\boldsymbol{\mu}_{\text{train}}^j$, $1 \leq j \leq n_{\text{train}}$. We will build the residual bases on each subdomain as: $\boldsymbol{\Phi}_i^r = \text{POD}(\mathbf{P}_i^r \mathbf{X}_g^r, \nu)$, $i = 1, \dots, n_{\Omega}$.

A.2 Greedy algorithm

Algorithm 4: Greedy algorithm to construct spatial sample sets of all subdomains Ω_i

Input: On each subdomain Ω_i : residual basis $\Phi_i^r \in \mathbb{R}^{n_i^r \times p_i^r}$, desired number of sample nodes n_i^z , number of working columns of Φ_i^r denoted by $n_i^c \leq \min(p_i^r, \gamma n_i^z)$, where γ denotes the number of unknowns at a node.

Output: Spatial sample set \mathfrak{s}_i on each subdomain Ω_i , $i = 1, \dots, n_\Omega$

- 1: **for** $i = 1 : n_\Omega$ {drop subscript i from this line for legibility} **do**
- 2: $\mathfrak{s} \leftarrow$ {corner nodes}
- 3: Compute the additional number of nodes to sample: $n^a = n^z - |\mathfrak{s}|$
- 4: Initialize counter for the number of working basis vectors used: $n^b \leftarrow 0$
- 5: Set the number of greedy iterations to perform: $n^{\text{it}} = \min(n^c, n^a)$
- 6: Compute the maximum number of right-hand sides in the least squares problems:
 $n^{\text{RHS}} = \text{ceil}(n^c/n^a)$
- 7: Compute the minimum number of working basis vectors per iteration: $n^{c,j,\text{min}} = \text{floor}(n^c/n^{\text{it}})$
- 8: Compute the minimum number of sample nodes to add per iteration: $n^{a,j,\text{min}} = \text{floor}(n^a n^{\text{RHS}}/n^c)$
- 9: **for** $j = 1, \dots, n^{\text{it}}$ {greedy iteration loop} **do**
- 10: Compute the number of working basis vectors for this iteration: $n^{c,j} \leftarrow n^{c,j,\text{min}}$
- 11: If $(j \leq n^c \bmod n^{\text{it}})$, then $n^{c,j} \leftarrow n^{c,j} + 1$
- 12: Compute the number of sample nodes to add during this iteration: $n^{a,j} \leftarrow n^{a,j,\text{min}}$
- 13: If $(n^{\text{RHS}} = 1)$ and $(j \leq n^a \bmod n^c)$, then $n^{a,j} \leftarrow n^{a,j} + 1$
- 14: **if** $j = 1$ **then**
- 15: $[R^1 \dots R^{n^{c,j}}] \leftarrow [\phi_r^1 \dots \phi_r^{n^{c,j}}]$
- 16: **else**
- 17: **for** $q = 1, \dots, n^{c,j}$ {basis vector loop}
- 18: $R^q \leftarrow \phi_r^{n^b+q} - [\phi_r^1 \dots \phi_r^{n^b}] \alpha$, with $\alpha = \underset{\gamma \in \mathbb{R}^{n^b}}{\text{argmin}} \| [\mathbf{Z} \phi_r^1 \dots \mathbf{Z} \phi_r^{n^b}] \gamma - \mathbf{Z} \phi_r^{n^b+q} \|_2$
- 19: **end for**
- 20: **end if**
- 21: **for** $k = 1, \dots, n^{a,j}$ {sample node loop} **do**
- 22: Choose node with largest average error: $n \leftarrow \arg \max_{l \notin \mathfrak{s}} \sum_{q=1}^{n^{c,j}} \left(\sum_{j \in \delta(l)} (R_j^q)^2 \right)$, where $\delta(l)$
denotes the degrees of freedom associated with node l .
- 23: $\mathfrak{s} \leftarrow \mathfrak{s} \cup \{n\}$
- 24: **end for**
- 25: $n^b \leftarrow n^b + n^{c,j}$
- 26: **end for**
- 27: **end for**

We adopt and adjust the original greedy algorithm developed earlier [37] to build the sample mesh for each subdomain Ω_i , $i = 1, \dots, n_\Omega$. Algorithm 4 presents the modified greedy algorithm in which we drop the subscript i of subdomains for avoiding cumbersomeness, and note that $[\phi_r^1 \dots \phi_r^{p_i^r}] = \Phi_i^r$ is the residual bases and $\mathbf{Z} = \mathbf{Z}_i$ is the sampling matrix of each subdomain Ω_i .

In comparison to the original greedy algorithm in [37], Algorithm 4 has two modifications: (i) there is an outer “for loop” that loops over all subdomains (line 1, algorithm 4), and (ii) we include the “corner” nodes (i.e., any interface node) into the sample mesh before the first greedy iteration (line 2, algorithm 4). The latter modification ensures that there is at least one interface node be included in the sample mesh, as otherwise $\hat{\mathbf{x}}_i^\Gamma$ (and hence $\tilde{\mathbf{x}}_i^\Gamma$) will not be updated through Newton iterations (since $\mathbf{p}_i^{\Gamma(k)}$ is always zero in (4.6)). Namely, there may have no connection between one subdomain with surrounding neighbor subdomains, or that subdomain is completely isolated. This phenomenon is called “digraph connecting condition” [59] (see figure 1 for an example of corner nodes of subdomains). We also note that the offline GNAT procedure is

performed only once as it only depends on the residual bases of each subdomain, and completely do *not* depend on basis types, constraint types and solver types of the DD-LSPG problem.

References

- [1] Maday, Y. and Rønquist, E. M., “A reduced-basis element method,” Journal of scientific computing, Vol. 17, No. 1-4, 2002, pp. 447–459.
- [2] Maday, Y. and Ronquist, E. M., “The reduced basis element method: application to a thermal fin problem,” SIAM Journal on Scientific Computing, Vol. 26, No. 1, 2004, pp. 240–258.
- [3] Iapichino, L., Quarteroni, A., and Rozza, G., “A reduced basis hybrid method for the coupling of parametrized domains represented by fluidic networks,” Computer Methods in Applied Mechanics and Engineering, Vol. 221, 2012, pp. 63–82.
- [4] Huynh, D. B. P., Knezevic, D. J., and Patera, A. T., “A static condensation reduced basis element method: approximation and a posteriori error estimation,” ESAIM: Mathematical Modelling and Numerical Analysis, Vol. 47, No. 1, 2013, pp. 213–251.
- [5] Eftang, J., Huynh, D., Knezevic, D., Ronquist, E., and Patera, A., “Adaptive port reduction in static condensation,” IFAC Proceedings Volumes, Vol. 45, No. 2, 2012, pp. 695–699.
- [6] Iapichino, L., Quarteroni, A., and Rozza, G., “Reduced basis method and domain decomposition for elliptic problems in networks and complex parametrized geometries,” Computers & Mathematics with Applications, Vol. 71, No. 1, 2016, pp. 408–430.
- [7] Benzi, M., Golub, G. H., and Liesen, J., “Numerical solution of saddle point problems,” Acta numerica, Vol. 14, 2005, pp. 1–137.
- [8] Huynh, D. B. P., Knezevic, D. J., and Patera, A. T., “A static condensation reduced basis element method: Complex problems,” Computer Methods in Applied Mechanics and Engineering, Vol. 259, 2013, pp. 197–216.
- [9] Løvgrén, A. E., Maday, Y., and Rønquist, E. M., “The reduced basis element method for fluid flows,” Analysis and Simulation of Fluid Dynamics, Springer, 2006, pp. 129–154.
- [10] Nguyen, N. C., “A multiscale reduced-basis method for parametrized elliptic partial differential equations with multiple scales,” Journal of Computational Physics, Vol. 227, No. 23, 2008, pp. 9807–9822.
- [11] He, W., Avery, P., and Farhat, C., “In-situ adaptive reduction of nonlinear multiscale structural dynamics models,” arXiv preprint arXiv:2004.00153, 2020.
- [12] Kaulmann, S., Ohlberger, M., and Haasdonk, B., “A new local reduced basis discontinuous Galerkin approach for heterogeneous multiscale problems,” Comptes Rendus Mathematique, Vol. 349, No. 23-24, 2011, pp. 1233–1238.
- [13] Ohlberger, M. and Schindler, F., “Error control for the localized reduced basis multiscale method with adaptive on-line enrichment,” SIAM Journal on Scientific Computing, Vol. 37, No. 6, 2015, pp. A2865–A2895.
- [14] Abdulle, A. and Henning, P., “A reduced basis localized orthogonal decomposition,” Journal of Computational Physics, Vol. 295, 2015, pp. 379–401.
- [15] Martini, I., Rozza, G., and Haasdonk, B., “Reduced basis approximation and a-posteriori error estimation for the coupled Stokes-Darcy system,” Advances in Computational Mathematics, Vol. 41, No. 5, 2015, pp. 1131–1157.

- [16] Buhr, A., Engwer, C., Ohlberger, M., and Rave, S., “ArbiLoMod, a simulation technique designed for arbitrary local modifications,” SIAM Journal on Scientific Computing, Vol. 39, No. 4, 2017, pp. A1435–A1465.
- [17] Barbič, J. and Zhao, Y., “Real-time large-deformation substructuring,” ACM transactions on graphics (TOG), Vol. 30, No. 4, 2011, pp. 1–8.
- [18] Kim, T. and James, D. L., “Physics-based character skinning using multidomain subspace deformations,” IEEE transactions on visualization and computer graphics, Vol. 18, No. 8, 2012, pp. 1228–1240.
- [19] Yang, Y., Xu, W., Guo, X., Zhou, K., and Guo, B., “Boundary-aware multidomain subspace deformation,” IEEE transactions on visualization and computer graphics, Vol. 19, No. 10, 2013, pp. 1633–1645.
- [20] Peiret, A., Andrews, S., Kövecses, J., Kry, P. G., and Teichmann, M., “Schur complement-based substructuring of stiff multibody systems with contact,” ACM Transactions on Graphics (TOG), Vol. 38, No. 5, 2019, pp. 1–17.
- [21] Teng, Y., Meyer, M., DeRose, T., and Kim, T., “Subspace condensation: full space adaptivity for subspace deformations,” ACM Transactions on Graphics (TOG), Vol. 34, No. 4, 2015, pp. 1–9.
- [22] Buffoni, M., Telib, H., and Iollo, A., “Iterative methods for model reduction by domain decomposition,” Computers & Fluids, Vol. 38, No. 6, 2009, pp. 1160–1167.
- [23] Toselli, A. and Widlund, O., Domain decomposition methods - algorithms and theory, Vol. 34, Springer Science & Business Media, 2006.
- [24] Sirovich, L., “Turbulence and the dynamics of coherent structures. Part I: Coherent structures,” Quarterly of applied mathematics, Vol. 45, No. 3, 1987, pp. 561–571.
- [25] Kerfriden, P., Gouy, O., Rabczuk, T., and Bordas, S.-A., “A partitioned model order reduction approach to rationalise computational expenses in nonlinear fracture mechanics,” Computer Methods in Applied Mechanics and Engineering, Vol. 200, No. 5, 2012, pp. 850–866.
- [26] Chaturantabut, S. and Sorensen, D. C., “Nonlinear model reduction via discrete empirical interpolation,” SIAM Journal on Scientific Computing, Vol. 32, No. 5, 2010, pp. 2737–2764.
- [27] Corigliano, A., Dossi, M., and Mariani, S., “Model Order Reduction and domain decomposition strategies for the solution of the dynamic elastic–plastic structural problem,” Computer Methods in Applied Mechanics and Engineering, Vol. 290, 2015, pp. 127–155.
- [28] Gravouil, A. and Combescure, A., “Multi-time-step explicit–implicit method for non-linear structural dynamics,” International Journal for Numerical Methods in Engineering, Vol. 50, No. 1, 2001, pp. 199–225.
- [29] Baiges, J., Codina, R., and Idelsohn, S., “A domain decomposition strategy for reduced order models. Application to the incompressible Navier–Stokes equations,” Computer Methods in Applied Mechanics and Engineering, Vol. 267, 2013, pp. 23–42.
- [30] Baiges, J., Codina, R., and Idelsohn, S., “Explicit reduced-order models for the stabilized finite element approximation of the incompressible Navier–Stokes equations,” International Journal for Numerical Methods in Fluids, Vol. 72, No. 12, 2013, pp. 1219–1243.
- [31] Bui-Thanh, T., Willcox, K., and Ghattas, O., “Model reduction for large-scale systems with high-dimensional parametric input space,” SIAM Journal on Scientific Computing, Vol. 30, No. 6, 2008, pp. 3270–3288.
- [32] LeGresley, P. A., Application of proper orthogonal decomposition (POD) to design decomposition methods, Stanford University, 2006.

- [33] Carlberg, K., Bou-Mosleh, C., and Farhat, C., “Efficient non-linear model reduction via a least-squares Petrov–Galerkin projection and compressive tensor approximations,” International Journal for Numerical Methods in Engineering, Vol. 86, No. 2, 2011, pp. 155–181.
- [34] Carlberg, K., Barone, M., and Antil, H., “Galerkin v. least-squares Petrov–Galerkin projection in nonlinear model reduction,” Journal of Computational Physics, Vol. 330, 2017, pp. 693–734.
- [35] Carlberg, K., Choi, Y., and Sargsyan, S., “Conservative model reduction for finite-volume models,” Journal of Computational Physics, Vol. 371, 2018, pp. 280–314.
- [36] Choi, Y. and Carlberg, K., “Space–Time Least-Squares Petrov–Galerkin Projection for Nonlinear Model Reduction,” SIAM Journal on Scientific Computing, Vol. 41, No. 1, 2019, pp. A26–A58.
- [37] Carlberg, K., Farhat, C., Cortial, J., and Amsallem, D., “The GNAT method for nonlinear model reduction: effective implementation and application to computational fluid dynamics and turbulent flows,” Journal of Computational Physics, Vol. 242, 2013, pp. 623–647.
- [38] Choi, Y., Coombs, D., and Anderson, R., “SNS: a solution-based nonlinear subspace method for time-dependent model order reduction,” SIAM Journal on Scientific Computing, Vol. 42, No. 2, 2020, pp. A1116–A1146.
- [39] Astrid, P., Weiland, S., Willcox, K., and Backx, T., “Missing point estimation in models described by proper orthogonal decomposition,” IEEE Transactions on Automatic Control, Vol. 53, No. 10, 2008, pp. 2237–2251.
- [40] Ryckelynck, D., “A priori hyperreduction method: an adaptive approach,” Journal of computational physics, Vol. 202, No. 1, 2005, pp. 346–366.
- [41] Everson, R. and Sirovich, L., “Karhunen–Loève procedure for gappy data,” Journal of the Optical Society of America A, Vol. 12, No. 8, 1995, pp. 1657–1664.
- [42] Halko, N., Martinsson, P.-G., and Tropp, J. A., “Finding structure with randomness: Probabilistic algorithms for constructing approximate matrix decompositions,” SIAM review, Vol. 53, No. 2, 2011, pp. 217–288.
- [43] Mascarenhas, W. F., “The divergence of the BFGS and Gauss Newton methods,” Mathematical Programming, Vol. 147, No. 1-2, 2014, pp. 253–276.
- [44] Lubin, M., Petra, C. G., and Anitescu, M., “The parallel solution of dense saddle-point linear systems arising in stochastic programming,” Optimization Methods and Software, Vol. 27, No. 4-5, 2012, pp. 845–864.
- [45] Pestana, J. and Wathen, A. J., “The antitriangular factorization of saddle point matrices,” SIAM Journal on Matrix Analysis and Applications, Vol. 35, No. 2, 2014, pp. 339–353.
- [46] Rees, T. and Scott, J., “A comparative study of null-space factorizations for sparse symmetric saddle point systems,” Numerical Linear Algebra with Applications, Vol. 25, No. 1, 2018, pp. e2103.
- [47] Grepl, M. A., Maday, Y., Nguyen, N. C., and Patera, A. T., “Efficient reduced-basis treatment of nonaffine and nonlinear partial differential equations,” ESAIM: Mathematical Modelling and Numerical Analysis, Vol. 41, No. 03, 2007, pp. 575–605.
- [48] Eftang, J. L. and Patera, A. T., “Port reduction in parametrized component static condensation: approximation and a posteriori error estimation,” International Journal for Numerical Methods in Engineering, Vol. 96, No. 5, 2013, pp. 269–302.
- [49] Masoudi, S. and Romano, F., “CFD Vienna blog,” <http://cfdblogvienna.blogspot.co.at/p/computational-fluid-dynamics.html>, Nov. 2015.

- [50] Amsallem, D., Zahr, M., Choi, Y., and Farhat, C., “Design optimization using hyper-reduced-order models,” Structural and Multidisciplinary Optimization, Vol. 51, No. 4, 2015, pp. 919–940.
- [51] Choi, Y., Oxberry, G., White, D., and Kirchdoerfer, T., “Accelerating design optimization using reduced order models,” arXiv preprint arXiv:1909.11320, 2019.
- [52] Choi, Y., Boncoraglio, G., Anderson, S., Amsallem, D., and Farhat, C., “Gradient-based constrained optimization using a database of linear reduced-order models,” Journal of Computational Physics, 2020, pp. 109787.
- [53] White, D. A., Choi, Y., and Kudo, J., “A dual mesh method with adaptivity for stress-constrained topology optimization,” Structural and Multidisciplinary Optimization, Vol. 61, No. 2, 2020, pp. 749–762.
- [54] Lee, K. and Carlberg, K. T., “Model reduction of dynamical systems on nonlinear manifolds using deep convolutional autoencoders,” Journal of Computational Physics, Vol. 404, 2020, pp. 108973.
- [55] Kim, Y., Choi, Y., Widemann, D., and Zohdi, T., “A fast and accurate physics-informed neural network reduced order model with shallow masked autoencoder,” arXiv preprint arXiv:2009.11990, 2020.
- [56] Hoang, K. C., Kerfriden, P., Khoo, B., and Bordas, S. P. A., “An efficient goal-oriented sampling strategy using reduced basis method for parametrized elastodynamic problems,” Numerical Methods for Partial Differential Equations, Vol. 31, No. 2, 2015, pp. 575–608.
- [57] Hoang, K., Fu, Y., and Song, J., “An hp-proper orthogonal decomposition–moving least squares approach for molecular dynamics simulation,” Computer Methods in Applied Mechanics and Engineering, Vol. 298, 2016, pp. 548–575.
- [58] Hoang, K. C., Kim, T.-Y., and Song, J.-H., “Fast and accurate two-field reduced basis approximation for parametrized thermoelasticity problems,” Finite Elements in Analysis and Design, Vol. 141, 2018, pp. 96–118.
- [59] GeeksforGeeks, “Check if a directed graph is connected or not,” <https://www.geeksforgeeks.org/check-if-a-directed-graph-is-connected-or-not/>, Dec. 2018.

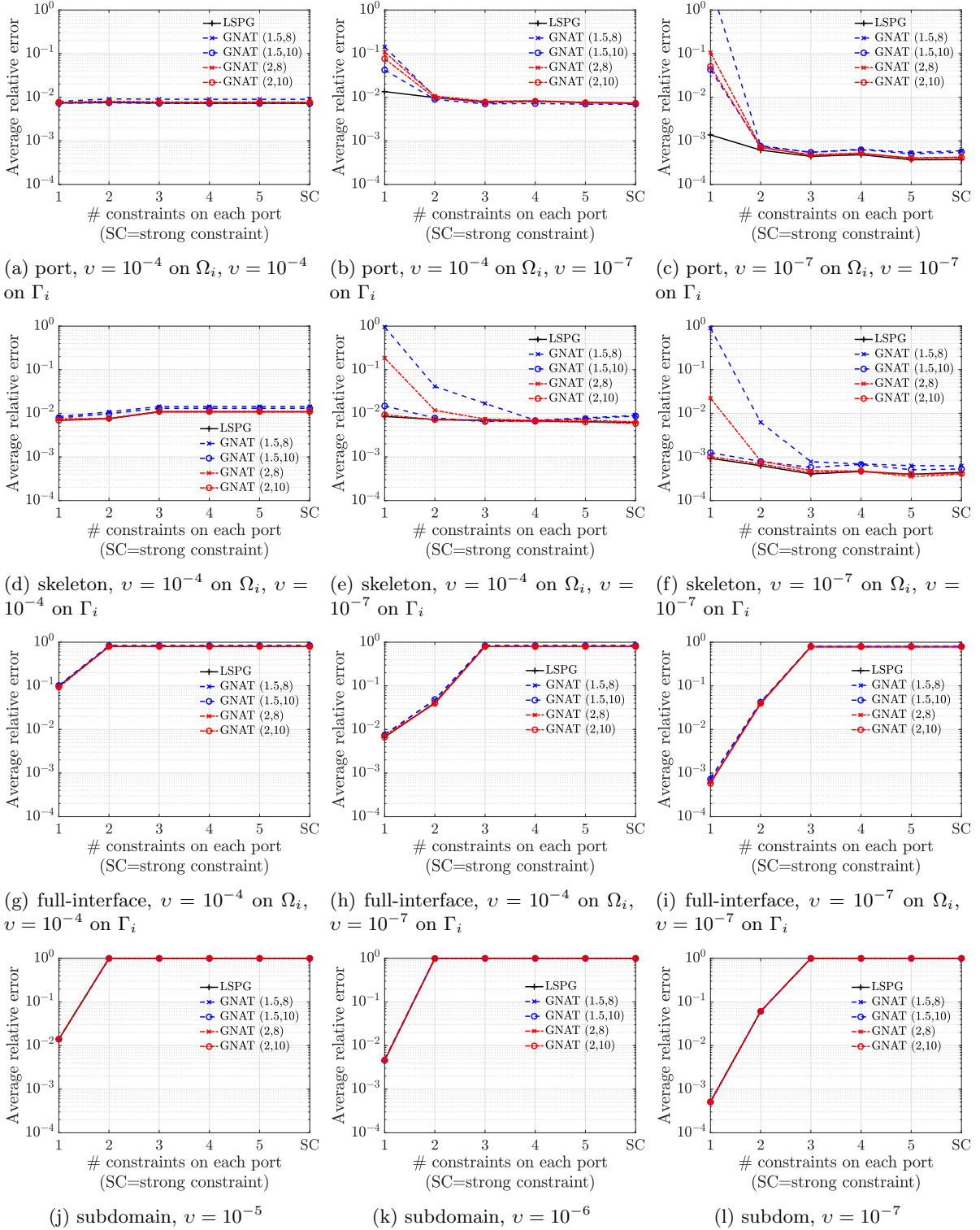


Figure 17: Burgers equation, 4x2 “fine” configuration, average relative error (DD-LSPG and GNAT) versus number of constraint per port for parameters reported in Table 19. In the legend GNAT(x, y) implies the GNAT model with $n_i^z/p_i^r = x$ and $v = 10^{-y}$ for r_i .